

10

A large narrow band H α survey at $z \sim 0.2$: the bright end of the luminosity function, cosmic variance and clustering across cosmic time

We carried out the largest ($> 3.5 \times 10^5 \text{ Mpc}^3$, 26 deg^2) H α narrow band survey to date at $z \sim 0.2$ in the SA22, W2 and XMMLSS extragalactic fields. Our survey covers a large enough volume to overcome cosmic variance and to sample bright and rare H α emitters up to an observed luminosity of $\sim 10^{42.4} \text{ erg s}^{-1}$, equivalent to $\sim 11 M_{\odot} \text{ yr}^{-1}$. Using our sample of 220 sources brighter than $> 10^{41.4} \text{ erg s}^{-1}$ ($> 1 M_{\odot} \text{ yr}^{-1}$), we derive H α luminosity functions, which are well described by a Schechter function with $\phi^* = 10^{-2.85 \pm 0.03} \text{ Mpc}^{-3}$ and $L_{\text{H}\alpha}^* = 10^{41.71 \pm 0.02} \text{ erg s}^{-1}$ (with a fixed faint end slope $\alpha = -1.35$). We find that surveys probing smaller volumes ($\sim 3 \times 10^4 \text{ Mpc}^3$) are heavily affected by cosmic variance, which can lead to errors of over 100 per cent in the characteristic density and luminosity of the H α luminosity function. We derive a star formation rate density of $\rho_{\text{SFRD}} = 0.0094 \pm 0.0008 M_{\odot} \text{ yr}^{-1}$, in agreement with the redshift-dependent H α parametrisation from Sobral et al. (2013). The two-point correlation function is described by a single power law $\omega(\theta) = (0.159 \pm 0.012)\theta^{(-0.75 \pm 0.05)}$, corresponding to a clustering length of $r_0 = 3.3 \pm 0.8 \text{ Mpc/h}$. We find that the most luminous H α emitters at $z \sim 0.2$ are more strongly clustered than the relatively fainter ones. The $L_{\text{H}\alpha}^*$ H α emitters at $z \sim 0.2$ in our sample reside in $\sim 10^{12.5-13.5} M_{\odot}$ dark matter haloes. This implies that the most star forming galaxies always reside in relatively massive haloes or group-like environments and that the typical host halo mass of star-forming galaxies is independent of redshift if scaled by $L_{\text{H}\alpha}/L_{\text{H}\alpha}^*(z)$, as proposed by Sobral et al. (2010).

Stroe & Sobral
MNRAS in press (2015)

Table 10.1: Area and volumes covered by the narrow band observations. Only the common area between the two filters is listed. The same area is used to calculate the co-moving volume.

Field	No pointings	Area deg ²	z	Volume 10 ⁴ Mpc ³
SA22	24	6.1	0.19	7.5
			0.22	9.8
W2	12	3.6	0.19	4.4
			0.22	5.7
XMMLSS	13	3.1	0.19	3.9
			0.22	5.0
Total	49 × 2	12.8 × 2		36.3

10.1 Introduction

The star formation (SF) activity in the Universe was significantly higher in the past, reaching a peak $\sim 10 - 11$ Gyrs ago ($z \sim 2 - 3$, e.g. Lilly et al. 1996; Karim et al. 2011; Bouwens et al. 2011; Gunawardhana et al. 2013; Sobral et al. 2013; Bouwens et al. 2015), and with the typical star formation rate (SFR) of galaxies (SFR*) at $z \sim 2$ being a factor ~ 10 times higher than at $z = 0$ (Sobral et al. 2014). However, the understanding of how and through which physical mechanisms the typical SFRs of galaxies have declined over the last 11 Gyrs is still poor.

In order to study SF across cosmic time, a number of tracers can be used. Ultra violet (UV) data can be used to trace radiation coming from massive, short-lived stars. Dust heated by the UV radiation emits in the far infra-red (FIR). The radiation from the massive stars also ionises the surrounding gas and leads to numerous recombination lines such as $H\alpha$ (6563Å) and [OII] (3727Å). Radio observations can be used to trace emission from super nova remnants. However, it is not trivial to combine these SF indicators, given they trace different phases of SF (averaged on short, ~ 10 Myr, or long, ~ 100 Myr, timescales, dust obscured, etc.), with different selection functions. Some selections are significantly biased: UV-selected samples miss dusty/metal enriched star forming galaxies, while the FIR exclusively selects dusty star-forming regions. Therefore, one of the main challenges in obtaining a complete picture of the SF evolution is the direct comparison of equally selected large samples of SF galaxies at a range of redshifts. Samples at high redshift tend to be obtained with a completely different selection than those at lower redshift, which can result in misinterpreted evolutionary trends which are more likely connected with the different selections at different redshifts than the actual evolution of galaxies across time (e.g. Stott et al. 2013).

An effective way of overcoming such limitations is by using a single technique and a single SF indicator up to the peak of the star formation activity. This can be achieved by tracing the $H\alpha$ emission line, which is one of the most sensitive and well-calibrated SF traces and also benefits from low intrinsic dust extinction within the host galaxy (when compared to e.g. UV). $H\alpha$ surveys performed using the narrow-band (NB) technique can provide clean, large and complete samples SF galaxies (c.f. Oteo et al. 2015).

A successful example of the NB technique put into practice is the High Redshift Emission Line Survey (HiZELS, Geach et al. 2008; Best et al. 2010; Sobral et al. 2013), but also see the

pioneering works of Bunker et al. (1995), Moorwood et al. (2000), Kurk et al. (2004), Ly et al. (2007) and Shioya et al. (2008). At $z \sim 1 - 2$, the volumes probed by HiZELS over a number of different fields ($\sim 5 - 10 \text{ deg}^2$) virtually overcome cosmic variance (Sobral et al. 2015b). However, at $z < 0.4$, the volumes probed over $1 - 2 \text{ deg}^2$ areas are only a minor fraction of those at high-redshift. Indeed, the samples at low redshift are greatly limited by cosmic variance, and even the widest surveys (e.g. Shioya et al. 2008, Cosmological Evolution Survey (COSMOS)) struggle to reach the characteristic $\text{H}\alpha$ luminosity ($L_{\text{H}\alpha}^*$). An additional limitation is saturation, which means missing the luminous population of $\text{H}\alpha$ emitters (with $> 1 - 3 M_{\odot} \text{ yr}^{-1}$, for discussion of this effect see Stroe et al. 2014). This can lead to an underestimation of $\text{H}\alpha$ luminosity function (LF) bright end and an exaggeration of the evolution of $L_{\text{H}\alpha}^*$ from high to low redshift.

The combination of all these issues and the different selection techniques applied by each study makes it extremely hard to fairly compare between $z < 0.4$ and $z > 1$ samples when based on the same surveys. While it is possible to use other samples at lower redshift (e.g. spectroscopic selection, Gunawardhana et al. 2013), the importance of using the same selection in order to obtain clean and clear evolutionary trends cannot be stressed enough: without the guarantee of a unique selection, any evolutionary trends become hard/impossible to understand and interpret, limiting our understanding.

In order to overcome the current shortcomings we clearly require a large $\text{H}\alpha$ survey at lower redshifts which can be directly matched to higher redshift. In this paper we present a large survey at $z \sim 0.2$, covering a similar co-moving volume ($3.5 \times 10^5 \text{ Mpc}^3$, spread over 3 independent fields to overcome cosmic variance) and complete down to similar luminosity limits relative to $L_{\text{H}\alpha}^*$ as surveys at $z > 1$. The structure of the paper is as follows: in Section 10.2 we present the observations and the reduction of the narrow-band data, while in Section 10.3 we show the selection of the $\text{H}\alpha$ emitters. Section 10.4 deals with the $z \sim 0.2$ $\text{H}\alpha$ luminosity function and Section 10.5 the clustering of bright $\text{H}\alpha$ sources and the implications of our results for the cosmic SF evolution are presented. We present concluding remarks in Section 10.6.

At the two redshifts probed, $z \sim 0.19$ and 0.22 , 1 arcsec covers a physical scale of 3.2 kpc and 3.6 kpc, respectively. The luminosity distance is $d_L \approx 940 \text{ Mpc}$ at $z \sim 0.19$ and $\approx 1110 \text{ Mpc}$ at $z = 0.22$. All coordinates are in the J2000 coordinate system. We use the Chabrier (2003) initial mass function (IMF) throughout the paper, and results from other studies are also converted to this IMF.

10.2 Observations & Data Reduction

We obtain NB data tracing $\text{H}\alpha$ at $z \sim 0.19$ and ~ 0.22 in three well studied extragalactic fields located at high Galactic latitude. W2 is part of the Canada-France-Hawaii Telescope Legacy Survey (CFHTLS) 155 deg^2 , wide and shallow survey (Gwyn 2012), aimed at studying the large scale structure and matter distribution using weak lensing and galaxy distribution. SA22 is part of the W4 field in CFHLS and multiwavelength data has been compiled by Matthee et al. (2014) and Sobral et al. (2015b). The XMM Large Scale Structure Survey (XMM-LSS, Pierre et al. 2004) is aimed at mapping large scale structures through clusters and groups of galaxies.

Table 10.2: Typical 3σ limiting magnitudes for the three fields (including the standard spread in values), for each filter. The depth for each pointing (and within each CCD of out of the four WFC CCDs) varies across the fields over the ranges reported in the third and last column.

Field	Filter	3σ mag
SA22	NB1	$17.5^{+0.4}_{-0.3}$
	NB2	$17.4^{+0.4}_{-0.3}$
W2	NB1	$16.8^{+1.5}_{-0.6}$
	NB2	$16.7^{+0.7}_{-0.4}$
XMMLSS	NB1	$17.7^{+0.4}_{-0.3}$
	NB2	$17.5^{+0.5}_{-0.3}$

10.2.1 Narrow band $H\alpha$ observations

We obtained narrow band data using the NOVA782HA and NOVA804HA (Stroe et al. 2014, 2015; Sobral et al. 2015a) filters on the Wide Wide Field Camera (WFC)¹ mounted on the Isaac Newton Telescope (INT, I13BN008, PI Sobral)². For brevity, we label the filters as NB1 (NOVA782HA) and NB2 (NOVA804HA). Given the central wavelengths of the filters are 7852.4\AA and 8036.15\AA , with a full-width-half-maximum (FWHM) of 110\AA , the two filters trace $H\alpha$ emission in the $z = 0.1865 - 0.2025$ and $z = 0.2170 - 0.2330$ redshift ranges. Note that given the large field of view of WFC, a slight blue shift in the filter central wavelength is expected at large off-axis distances. However, given the WFC focal ratio ($f/3.29$), this effect is expected to be very low (a few per cent Bland-Hawthorn et al. 2001). Sobral et al. (2015a) and Stroe et al. (2015) characterised the filters with spectroscopy from the Keck and William Herschel Telescopes with sources located both towards and away from the pointing centre and found that the redshift distribution of $H\alpha$ emitters matches that expected from the filter profile, without any noticeable offset.

Observations were conducted in five bright nights, between 22 and 26 of October 2013, under ~ 1 arcsec seeing conditions. A five-position dither pattern was employed for the individual exposures (of 600 s each) to cover the spacings between the four WFC CCDs. Forty-nine individual pointings (of $\sim 0.3 \text{ deg}^2$ each with WFC) split between the three fields (SA22, W2 and XMMLSS) cover an area of almost 13 deg^2 at each of the two redshifts (thus an effective area of $\sim 26 \text{ deg}^2$ combined), tracing a total co-moving volume of about $3.63 \times 10^5 \text{ Mpc}^3$. The overlap with the multiwavelength data extends to about 10 deg^2 per redshift.

10.2.2 Narrow band data reduction

We reduce the data using the PYTHON based pipeline described in Stroe et al. (2014). In short, we median combine the sky flats and biases and use the stacks to correct the science data. After detecting sources using the SExtractor package (Bertin & Arnouts 1996) and masking them in each science exposure, we median combine the exposures to obtain a ‘super-flat’. We divide the data through the ‘super-flat’ to correct for ‘fringing’. We then use SCAMP (Bertin 2006)

¹http://www.ing.iac.es/engineering/detectors/ultra_wfc.htm

²<http://www.ing.iac.es/Astronomy/telescopes/int/>

to find astrometric solutions for the science exposures. The exposures are normalised to the same zero-point (ZP) by comparison to the red magnitude in the fourth United States Naval Observatory (USNO) Catalog (UCAC4; Zacharias et al. 2013). We combine the processed data into final stacked images using SWARP (Bertin et al. 2002). We photometrically calibrate our data against the *i* band magnitude from the Sloan Digital Sky Survey (SDSS) Data Release 9 (SDSS DR9 Ahn et al. 2012), which covers all our fields (SA22, W2 and XMMLSS). We extract magnitudes within 5 arcsec apertures using SExtractor (Bertin & Arnouts 1996). This corresponds to a physical diameter of ~ 18 kpc at ~ 0.2 redshift.

We calculate 3σ limiting magnitudes using the RMS noise reported by SExtractor (see Table 10.2). The depth of the observations varies across the pointings and even between the different chips of the WFC. Hence, we calculate the RMS noise individually for each CCDs, for each pointing, across the three fields.

We apply the NB technique to select line emitters, using a NB filter tracing line emission within a narrow range in redshift, in combination with another NB or broad band (BB) filter used for the estimation of the continuum emission underlying the emission line. We use two NB filters to trace $H\alpha$ emission in two redshift ranges (0.1865 – 0.2025 and 0.2170 – 0.2330). For each NB filter, we use the other NB filter to estimate the continuum BB emission. In this way, for line emitters, one NB filter captures the BB emission as well as the line emission, while the other NB filter only captures the stellar continuum emission. Our method is similar to that of Dale et al. (2010), who use twin NB filters for continuum subtraction. In further text, we use labels according to the filter which was used as NB filter in that particular case. Therefore, when we label with NB1, we refer to line-emitters in the 0.1865 – 0.2025 redshift range, while NB2 refers to the 0.2170 – 0.2330 range. The details of the selection method are laid down in Section 10.3.2.

10.2.3 Optical and IR data

In our analysis, we use the rich multi-wavelength optical and infra-red (IR) data available for the SA22, W2 and XMMLSS fields.

All three fields are part of the CFHTLS wide and shallow surveys (SA22, W2 and XMMLSS are in fields W4, W2 and W1). We make use of the *g*, *r*, *i* and *z* photometry (Erben et al. 2013) and photometric redshifts (Ilbert et al. 2006) available through the CFHTLS T0007 release.

We also employ near IR data in the *J* and *K_s* filters, down to magnitude ~ 21.2 and ~ 20.0 respectively, obtained as part of the Visible and Infrared Survey Telescope for Astronomy (VISTA) Hemisphere Survey (VHS, McMahon and the VHS Collaboration, 2012, in preparation). Where available, in the XMMLSS field, we preferentially use data from the VISTA Deep Extragalactic Observations (VIDEO) Survey (Jarvis et al. 2013), which is about 3.5 magnitudes deeper than VISTA. We also make use of the IR photometric data taken in the SA22 field as part of the second data release of the UKIDSS Deep Extragalactic Survey (Warren et al. 2007), which reaches magnitudes 23.4 and 22.8 in the *J* and *K_s* bands, respectively, with a catalogue from Sobral et al. (2015b).

We make use of the photometric and spectroscopic redshift compilation in the UKIDSS Ultra Deep Survey (part of XMMLSS) available as part of their 8th data release³, as well as

³<http://www.nottingham.ac.uk/astronomy/UDS/data/data.html>

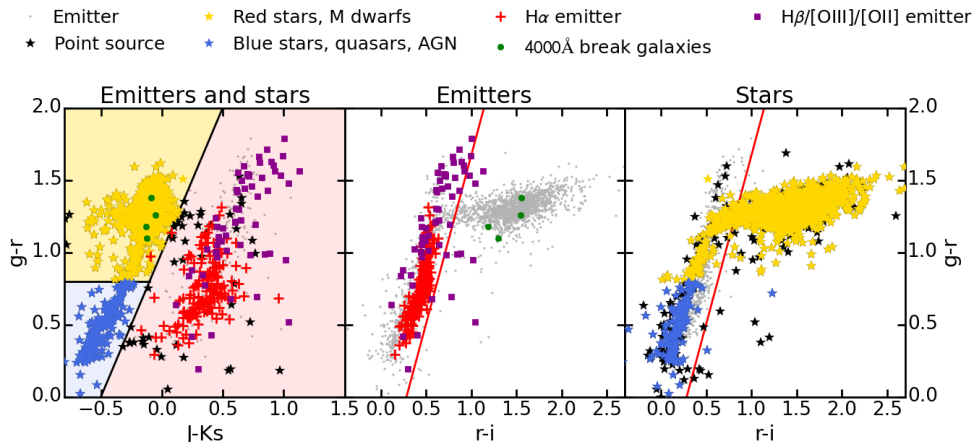


Figure 10.1: Colour-colour plots for the SA22, W2 and XMMLSS fields, mainly used to remove stars. The first plot shows $g-r$ versus $J-Ks$ while the middle and last plots show $g-r$ versus $r-i$. We first separate stars and emitters using the $g-r$ versus $J-Ks$, and the apply an extra cut using the optical colours to further remove stars with absorption features in one of the filter. The solid red and black lines display the colour cuts used to select point-like objects. $H\alpha$ emitters are plotted in red crosses, while point-like sources are plotted as stars. 4000Å break galaxies are plotted in green crosses and high redshift sources in purple crosses.

other publicly available spectroscopy in the XMMLSS field (Garcet et al. 2007; Polletta et al. 2007; Tajer et al. 2007; Melnyk et al. 2013).

10.3 Methods and selecting the $H\alpha$ samples

Once sources are detected in the NB images, we cross-match the NB catalogues with the optical and IR catalogues presented in Section 10.2.3, using a 1 arcsec positional tolerance. Note that because the BB catalogues are deeper than our data by at least 2 mag, we have 100 per cent optical and IR coverage in the areas we have FOV overlap with all the multiwavelength data. We use each NB catalogue as base catalogue for the cross-match.

10.3.1 Star removal

As explained in Section 10.2.2, we use the two NB filters to trace $H\alpha$ emission at two redshifts ranges (0.1865 – 0.2025 and 0.2170 – 0.2330). However, given the wavelength coverage of the two adjacent filters our samples of line emitters is contaminated by stars (see also Stroe et al. 2014). Stars could mimic having an emission line if they have extremely red or a broad absorption feature, which would lead to a strong colour between the two NB filters. We expect the line emitters selected in the NB2 filter to be particularly contaminated with a population of (L, M) dwarf stars (Kirkpatrick et al. 1991, 1999). They will be selected as having excess in NB2 because their continuum has a broad absorption feature falling within the NB1 filter, leading to an underestimation of the continuum emission. The extremely red BB colours of these sources are also consistent with them being red dwarfs.

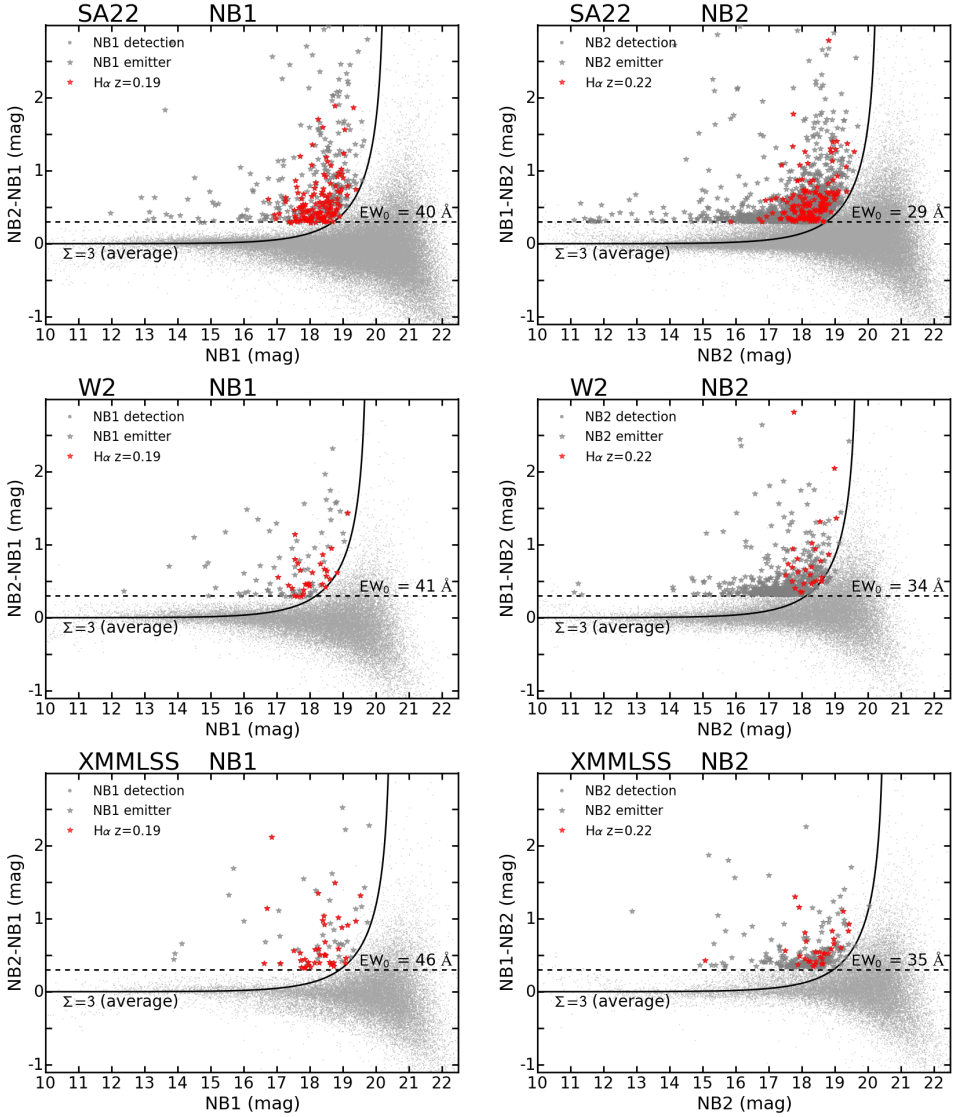


Figure 10.2: Colour-magnitude diagrams showing the excess as function of NB magnitude. The selection is performed separately for each CCD/pointing, field and NB filter, using the other NB filter for continuum estimation. Each panel is labelled with the corresponding field and the filter which is used as NB. The curves show average 3Σ colour significances for the average depth, as the RMS value varies between the pointings and CCDs. The horizontal dashed, black lines represent the intrinsic EW cuts. Note that we correct for incompleteness arising from our slightly different EW and colour significance cuts.

Table 10.3: Number of line emitters and $H\alpha$ emitters selected in each field and filter. We also list the average limiting observed $H\alpha$ luminosity at 50 per cent completeness and the equivalent SFR (using equation 10.11).

Field	Filter	Emitters	$H\alpha$ emitters	$\log(L_{H\alpha})$ (erg s^{-1})	SFR ($M_{\odot} \text{ yr}^{-1}$)
SA22	NB1	153	59	41.4	1.1
	NB2	238	91	41.4	1.1
W2	NB1	33	13	41.4	1.1
	NB2	55	15	41.6	1.7
XMMLSS	NB1	51	23	41.1	0.5
	NB2	50	19	41.4	1.1
Total	both	576	220		

We exclude stars using a colour-colour selection criterion using optical and IR colours based on Sobral et al. (2012), keeping in mind the distribution of sources in the colour-colour diagram. This is illustrated in Figure 10.1.

Red stars are selected using:

$$(g-r) > 2(J-Ks) + 1 \quad \& \quad (g-r) > 0.8 \quad \& \quad (J-Ks) > -0.7 \quad (10.1)$$

We select dwarf stars via:

$$(g-r) > (7/3)(r-i) - 2/3 \quad \& \quad (g-r) > 1.0 \quad (10.2)$$

Optically blue stars and dwarf stars with absorption features are selected by:

$$(g-r) > 2(J-Ks) + 1 \quad \& \quad (g-r) < 0.8 \quad (10.3)$$

We additionally use the ‘StarGal’ parameter in the CFHTLS photometric redshift catalogue to select stars (Ilbert et al. 2006), which categorises sources as point-like or extended objects.

Thus, in summary, we label sources as stars if:

- Source passes the red star selection criterion (equation 10.1) or
- Source passes the blue star selection criterion (equation 10.3) or
- Source passes the dwarf star selection criterion (equation 10.2) or
- Source is classified as star by the CFHTLS ‘StarGal’ parameter.

About 60–80 per cent of the sources mimicking emission lines are marked as stars. Spectroscopic observations using NB1 and NB2 (e.g Stroe et al. 2015; Sobral et al. 2015a) confirm the presence of such stars. All the sources masked as stars are removed from catalogues such that they are not selected as line emitters.

10.3.2 Selection of line emitters

We use the formalism developed by Bunker et al. (1995), which is widely used in the literature (e.g. Shioya et al. 2008; Sobral et al. 2009; Stroe et al. 2014) to select large numbers of line emitters. We refer the interested readers to those papers for the details of the selection criteria.

We select line emitters separately in each field and each NB filter. For brevity, in the following equations, we label the filter used to select emitters as NB, while we name the other NB filter, used to quantify the continuum emission, as BB filter. Note that we attempted the selection of line emitters using the i band filter, following Stroe et al. (2014) and Stroe et al. (2015). However, the relatively deep CFHTLS data becomes saturated at magnitude 17–18 and would prevent the selection of bright line emitters. Therefore using each NB filter for continuum subtraction of the other represents the optimal strategy, enabling the selection of line emitters up to magnitude 10. Using much deeper broad band i data would allow us to probe down to fainter emitters, but our aim for the paper is to study the bright population. By comparison, the widest $H\alpha$ survey at $z \sim 0.2$ to date, performed by Shioya et al. (2008), can only probe sources as bright as ~ 18 mag, but excels at the faint end (going down to 24 mag).

We select emitters in each NB filter based on their excess emission compared to the BB emission (quantified using the other NB filter). We first correct for any systematic colour offset between the two NB filters. Colour is defined here as the difference in magnitude between the filter used as NB and the filter used to measure broad band. We estimate a median offset of this colour, based on the scatter in the colours at non-saturated, but still bright NB magnitudes. We then apply this correction to the colour and the NB magnitude. However, because the filters are close in wavelength this correction is small (0.02 and 0.03 mag, for NB1 and NB2 respectively).

The excess emission is then quantified through the colour excess significance Σ , which is used to separate sources with real colour excess, compared to excess caused by random scatter (Sobral et al. 2009; Sobral et al. 2012):

$$\Sigma = \frac{10^{-0.4(m_{BB}-m_{NB})}}{10^{-0.4(ZP_{AB}-m_{NB})} \sqrt{\pi r^2 (\sigma_{NB}^2 + \sigma_{BB}^2)}}, \quad (10.4)$$

where ZP_{AB} is the magnitude system zero-point, m_{NB} and m_{BB} are the NB and BB magnitudes (where NB is the filter used for detection of line emitters and BB is the other NB filter used for quantifying the continuum emission), r is the radius of the aperture in pixels and σ_{NB} and σ_{BB} are the rms noise levels.

The NB or BB flux $f_{NB, BB}$ are calculated as:

$$f_{NB, BB} = \frac{c}{\lambda_{NB, BB}^2} 10^{-0.4(m_{NB, BB} - ZP_{AB})}, \quad (10.5)$$

where c is the speed of light, λ_{NB} and λ_{BB} are the central wavelengths of the two NB filters and $ZP_{AB} = 48.574$ is the ZP of the AB magnitude system. The line flux is:

$$F_{\text{line}} = \Delta \lambda_{NB} (f_{NB} - f_{BB}). \quad (10.6)$$

Note that the two filters are independent, hence there is no overlap in wavelength between NB1 and NB2. Therefore, if one filter captures line emission on top of the continuum, automatically the other NB filter picks up only continuum emission. Therefore, the line flux formula accounts for the fact the filter used as BB does not contain any line emission.

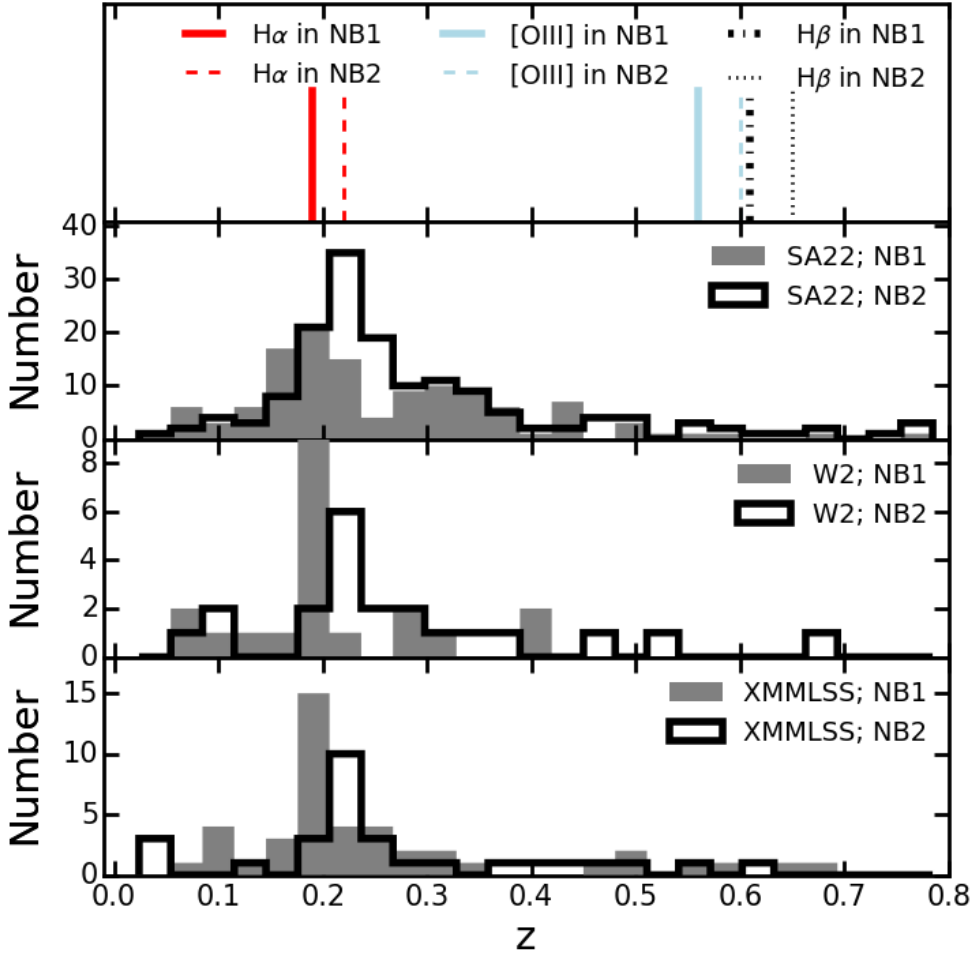


Figure 10.3: Photometric redshift distribution of line emitters for each field. Note the quality of the photometric redshifts varies between the fields. The top panel shows the main line we expect to capture with out two narrow band filters. The distribution contains clear peaks around $z \sim 0.2$, indicating our sample is dominated by $H\alpha$ emitters, with little contamination from higher redshift emitters.

We use the Σ parameter in conjunction with an equivalent width (EW) cut, which ensures that we select only sources which have a ratio of the line to continuum flux larger than the scatter at bright magnitudes. The observed EW is defined as:

$$EW = \Delta\lambda_{NB} \frac{f_{NB} - f_{BB}}{f_{BB}}, \quad (10.7)$$

where $\Delta\lambda_{NB} = 100 \text{ \AA}$ is the FWHM of the NB filters, while f_{NB} and f_{BB} are the NB and continuum fluxes. Note this formula is a simplified version of those presented in, e.g., Bunker et al. (1995) and Sobral et al. (2009), because we do not expect our BB filter to contain any emission line flux.

In the restframe of the sources, the intrinsic EW_0 is:

$$EW_0 = EW / (1 + z). \quad (10.8)$$

In conclusion, we select sources as emitters if:

- Their colour significance Σ is higher than 3 and
- Their equivalent width is higher than 3σ , where σ is the colour excess (BB-NB) scatter at bright, but not saturated magnitudes.

The $\Sigma = 3$ colour significance and the 3σ excess depend on the depth of the observations in each field (See Figure 10.2). We choose to not impose a single, common cut, to follow the natural depth of the data, rather than cutting the sample at excessively high EW and Σ . However, we note that we fully correct for the sources missed by our cuts, as explained in Section 10.4.1.

10.3.3 Selection of H α candidates

The line emitter population is made of H α emitters at $z \sim 0.2$, as well as higher redshift line emitters: H β ($\lambda_{\text{rest}} = 4861 \text{ \AA}$), [OIII] $\lambda\lambda 4959, 5007$ emitters at $z \sim 0.61 - 0.65$ and [OII] ($\lambda_{\text{rest}} = 3727 \text{ \AA}$) emitters at $z \sim 1.15$ (see Figure 10.3). Our sample could be contaminated by a population of 4000 \AA break galaxies at $z \sim 0.8$. As shown in Stroe et al. (2014), at $\sim 8000 \text{ \AA}$ and lower line fluxes, the line emitter population is dominated by [OII] $\lambda 3727$ emitters and $z \sim 0.8$ 4000 \AA break galaxies. However, at high fluxes, the number of H α and H β /[OIII] steeply rises, each amounting to about 50 per cent of the line emitter population. Therefore, given the shallow depth of our survey, we are strongly biased against detecting high-redshift ($z > 0.6$) sources. We expect the H α emitters to amount to about half of the emitter population. Figure 10.3, presenting the photometric redshift distribution of the line emitters, confirms these findings. The steps we undertake to robustly separate the H α emitters from the other sources are described in the following paragraphs.

We first visually inspected all line emitter candidates to flag any spurious sources coming from noisy edge regions of the chips or from false detections within the haloes of bright sources.

H α emitters are selected in the following way:

- The photometric or spectroscopic redshift of the source does not lie in the expected ranges for H β /[OIII]/[OII] emitters ($0.37 < z < 0.7$ and $0.9 < z < 1.2$) and 4000 \AA break galaxies ($0.7 < z < 0.9$) and

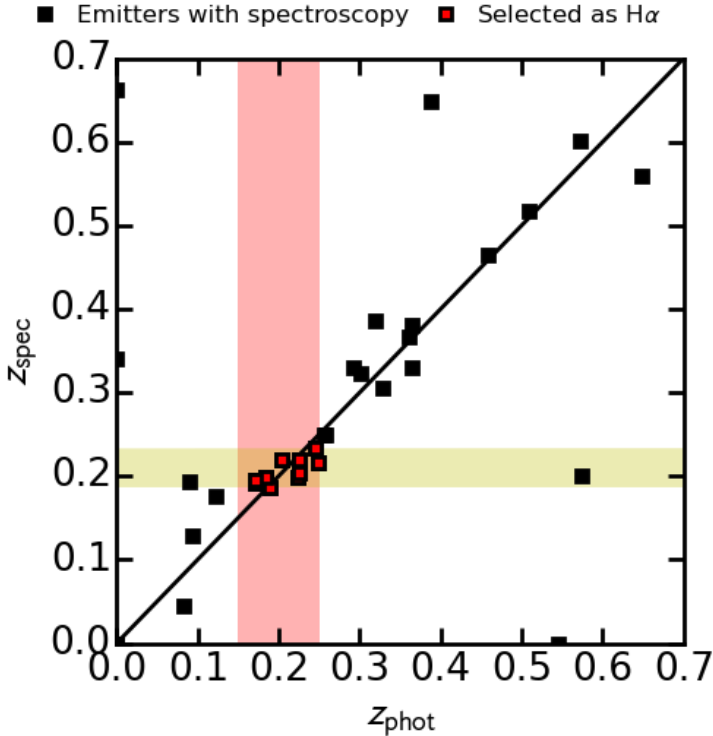


Figure 10.4: Photometric versus spectroscopic redshift for sources selected as emitters. The shaded red area indicates sources which based on their photometric redshift were selected as $H\alpha$. The yellow shaded area indicates the redshift range captured by the filters.

- The photometric or spectroscopic redshift of the source lies in the $0.15 < z < 0.25$ range.

Figure 10.1 displays the colour-colour distribution of line emitters, the cut employed to separate the source types and highlights the location of the $H\alpha$ emitters. All three fields and both filters are shown in the same plot. Separating the data per field and filter results in colour-colour diagrams which are consistent with Figure 10.1, indicating there are no systematic differences between the populations selected with the two NB filters. The number of $H\alpha$ emitters selected in each field can be found in Table 10.3, amounting to a total of 220 $H\alpha$ emitters. This amounts to almost 40 per cent of the total number of emitters, as expected and explained in Section 10.3.3.

Purity of the $H\alpha$ sample

We compare the spectroscopic and photometric redshifts in order to study the purity of the $H\alpha$ sample (Figure 10.4). We find that the photometric redshifts are within 0.05 of the spectroscopic ones. From the sources spectroscopically confirmed to be at lower or higher redshift, none make it into the $H\alpha$ catalogue, implying a very low contamination. Note that the range we used for selecting sources as $H\alpha$ from photometric redshifts is $0.15 - 0.25$, which is large enough to capture $H\alpha$ emitters in both filters, while minimising contamination. Out of

12 spectroscopically confirmed emitters we miss two sources, implying completeness higher than 80 per cent. However, the spectroscopy is limited and the low number statistics could lead to an overestimation or underestimation of the completeness and contamination. Future spectroscopic observations will allow us to further investigate this.

10.4 $H\alpha$ luminosity function and star-formation rate density

We use the sample of 220 $H\alpha$ sources to build luminosity functions.

Our filters are sensitive not only to $H\alpha$, but also to the adjacent [NII] double (6450 and 6585 Å) forbidden line. We subtract the [NII] contribution from the line fluxes using the method from Sobral et al. (2012) to obtain $H\alpha$ fluxes ($F_{\text{H}\alpha}$), which has been spectroscopically confirmed by Sobral et al. (2015b). The average [NII] contribution is about 30 per cent of the total line flux.

After we obtain pure $H\alpha$ fluxes $F_{\text{H}\alpha}$, we calculate the $H\alpha$ luminosity $L_{\text{H}\alpha}$:

$$L_{\text{H}\alpha} = 4\pi d_L^2(z) F_{\text{H}\alpha}, \quad (10.9)$$

where $d_L(z)$ is the luminosity distance (940 Mpc for the NB1 filter and 1110 Mpc for NB2).

10.4.1 Completeness, volume and filter profile corrections

We use the method of Sobral et al. (2012) to correct for the incompleteness arising from missing sources with faint $H\alpha$ fluxes and/or low EW . We select random samples of sources passing the selection criteria for being located at the redshifts traced by the two filters, but which are not selected as $H\alpha$ emitters. Fake $H\alpha$ emission lines are added to these sources which are then passed through the $H\alpha$ selection criteria (EW and Σ) described at the end of Section 10.3.3.

Because of the different depth between the pointings and between the four CCD chips, we independently study the recovery rate as function of the $H\alpha$ flux for each chip, pointing, filter and field. The results of the completeness study can be found in the Appendix in Figure 10.15. Our results are corrected for the effects of incompleteness, especially the $H\alpha$ luminosity function (see Sections 10.4.3 and 10.4.4 and, e.g., Figures 10.5, 10.6 and 10.7).

The volumes probed in each field and at each redshift assuming that the filters have a perfect top-hat shape are listed in Table 10.1. The total co-moving volume probed is 3.63×10^5 Mpc³, by far the largest volume ever surveyed in $H\alpha$ at $z \sim 0.2$. However, since the filter transmission does not follow perfectly an idealised top hat, we follow the method of Sobral et al. (2009) and Sobral et al. (2012) and correct the volumes to account for sources missed at the edges of the filter.

10.4.2 Survey limits

A 50 per cent completeness (see Figure 10.15) translates to average limiting $H\alpha$ luminosities of $10^{41.1-41.6}$ erg s⁻¹ for our survey. This is equivalent to limiting star formation rates (SFR) of $0.5 - 1.8 M_{\odot} \text{ yr}^{-1}$, with no intrinsic dust extinction applied. If 1 magnitude of dust extinction is applied this is equivalent to $0.2 - 0.8 \text{ SFR}^*$ (see equation 10.11 in Section 10.4.4).

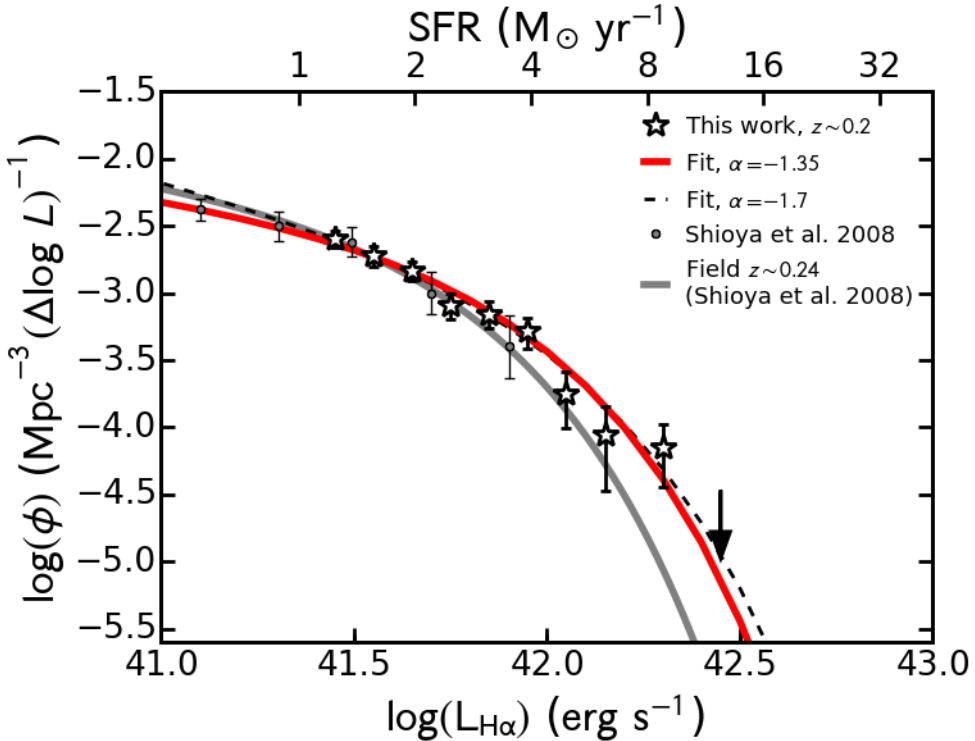


Figure 10.5: The $H\alpha$ luminosity function at $z \sim 0.2$ from our study and the best fit Schechter function. The $L_{H\alpha}$ is not corrected for intrinsic dust attenuation. For comparison, the results from Shioya et al. (2008) are also shown. Note the excellent agreement between the data in the overlapping luminosity range. However, our data probes brighter luminosities, enabling the first determination of the bright end of the $H\alpha$ luminosity function at $z \sim 0.2$.

Table 10.4: Best fit luminosity function at $z \sim 0.2$ obtained from combining data in the three fields (SA22, W2 and XMMLSS) and two NB filters. Since our data is not very deep, but probes the bright-end really well, we fix the faint-end slope α at two values. For comparison, we also list the results and volumes probed from other studies at a similar redshift. Note that none of the $L_{H\alpha}^*$ are corrected for $H\alpha$ extinction.

Source	z	V (10^4 Mpc^3)	α	$\log \phi^*$ (Mpc^{-3})	$\log L_{H\alpha}^*$ (erg s^{-1})
This study	~ 0.2	36.3	-1.35	-2.85 ± 0.03	41.71 ± 0.02
			-1.70	-3.06 ± 0.04	41.83 ± 0.03
Shioya et al. (2008)	~ 0.24	3.1	$-1.35^{+0.11}_{-0.13}$	$-2.65^{+0.27}_{-0.38}$	$41.54^{+0.38}_{-0.29}$
Ly et al. (2007)	~ 0.24	0.5	-1.70 \pm 0.10	-2.98 ± 0.40	41.25 ± 0.34
Drake et al. (2013)	~ 0.25	1.2	$-1.03^{+0.17}_{-0.15}$	$-2.53^{+0.17}_{-0.21}$	$40.83^{+0.19}_{-0.16}$

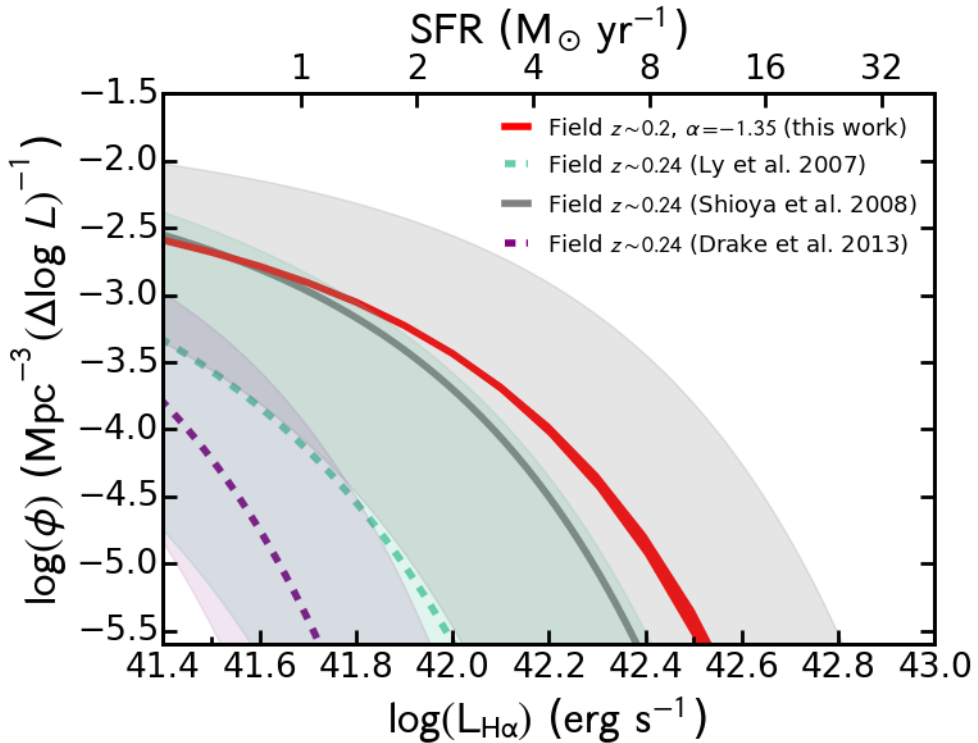


Figure 10.6: A range of luminosity functions at $z \sim 0.2$, from the current work and the works of Shioya et al. (2008), Ly et al. (2007) and Drake et al. (2013). In shaded areas, we overplot the ranges allowed by the 1σ error bars of the LF parameters. The works of Shioya et al. (2008), Ly et al. (2007) and Drake et al. (2013) explore the faint end part of the luminosity. The shaded areas indicate the 1σ uncertainties of the Schechter function parameters. Our measurements are consistent with previous work, but significantly improve the previously unexplored bright end. While our measurement error is given by cosmic variance, as shown in Section 10.4.6. However the other measurement do not include the error given by cosmic variance, which would add an error of about 100–200 per cent in the parameters.

The maximum observed $H\alpha$ luminosity our survey probes is $\sim 10^{42.4}$ erg s $^{-1}$, equivalent to SFRs of $11 M_{\odot} \text{ yr}^{-1}$ (or $\geq 27 M_{\odot} \text{ yr}^{-1}$ if 1 mag of dust extinction is applied). By comparison, the widest $H\alpha$ survey at a similar redshift, performed by Shioya et al. (2008), reaches $\sim 10^{41.9}$ erg s $^{-1}$, or $3.5 M_{\odot} \text{ yr}^{-1}$ ($8.7 M_{\odot} \text{ yr}^{-1}$ with dust extinction). This means our survey probes galaxies more than three times more star forming than previous surveys.

10.4.3 $H\alpha$ luminosity function

Using our final sample of $H\alpha$ emitters, we build luminosity functions (LF) which characterise the density of sources at any given $H\alpha$ luminosity. To do so, we bin sources based on their luminosity (corrected for the [NII] contribution, Section 10.4, but not for intrinsic dust extinction), by adding their associated inverse co-moving volume, corrected for the real filter profile

and incompleteness (as shown in Section 10.4.1).

We fit the binned data with a Schechter (1976) parametrisation:

$$\phi(L_{H\alpha})dL_{H\alpha} = \phi^* \left(\frac{L_{H\alpha}}{L_{H\alpha}^*} \right)^\alpha e^{-\frac{L_{H\alpha}}{L_{H\alpha}^*}} d\left(\frac{L_{H\alpha}}{L_{H\alpha}^*} \right), \quad (10.10)$$

where $L_{H\alpha}^*$ is the characteristic $H\alpha$ luminosity, ϕ^* is the characteristic density of $H\alpha$ emitters and α is the faint-end slope of the LF. Since our data is not deep enough to properly constrain the faint end slope of the LF (see Table 10.3), we fix α to two values previously derived in the literature using deep data: -1.35 from Shioya et al. (2008) and -1.7 from Ly et al. (2007). In fitting the LFs, we assume Poissonian errors.

Our best fit $H\alpha$ LF is described by a typical luminosity $\log(L_{H\alpha}^*) = 10^{(41.71 \pm 0.02)} \text{ erg s}^{-1}$ and a characteristic density $\log(\phi^*) = 10^{(-2.85 \pm 0.03)} \text{ Mpc}^{-3}$ (see Table 10.4 and Figure 10.5). Our data samples really well the bright-end of the LF, which enables us to place tight constraints on ϕ^* and $L_{H\alpha}^*$ (errors lower than 15 per cent). However, we lack depth (lowest bin at $\sim 10^{41.4} \text{ erg s}^{-1}$), so we fix the faint-end slope to -1.35 , as obtained by Shioya et al. (2008) from the previously widest $H\alpha$ survey, which benefits from high-quality, deep data reaching luminosities of $10^{39.3} \text{ erg s}^{-1}$, but is limited at the bright end. Therefore, the two surveys are highly complementary. Within the overlapping regions with data from both the Shioya et al. (2008) and our survey, the measurements are in excellent agreement. However, our LF, constrained up to $L_{H\alpha} = 10^{42.5} \text{ erg s}^{-1}$, indicates a slightly larger value of $L_{H\alpha}^*$, but still consistent with Shioya et al. (2008) within their large error bars (see Figure 10.6). Note that their uncertainties do not include the error from cosmic variance, which can result in 100–200 errors in the parameters of the LF (see Section 10.4.6). Any discrepancy between the results can be explained by cosmic variance, given Shioya’s volume is ~ 10 times smaller than ours and probes a single field. The differences between the ϕ^* results could also be explained by the different colour-colour methods used to separate the $H\alpha$ emitters from higher redshift line emitters.

The discrepancy with other studies is much larger however (see Figure 10.6). Compared to our results, Ly et al. (2007), slightly overestimate ϕ^* (not significant) and underestimate $L_{H\alpha}^*$ (at the 2σ level). Drake et al. (2013) obtain an $L_{H\alpha}^*$ which is highly underestimated ($10^{40.83} \text{ erg s}^{-1}$). The difference to our value is significant at the 11σ level. This is entirely driven by Drake’s small volume (~ 30 times smaller than ours) and the long exposures they were using in their study which prevented the study of sources brighter than 20 mag in the NB filter. Given the large variations in the LF parameters from cosmic variance, we expect all these results to be consistent with our measurement, once the cosmic variance error is folded in (see Section 10.4.6).

10.4.4 Star formation rate density

We can calculate the star formation rate density (SFRD) at $z \sim 0.2$ by integrating the luminosity function and converting $H\alpha$ luminosity to SFR. We use the $L_{H\alpha}$ to SFR conversion from Kennicutt (1998), corrected for the Chabrier (2003) IMF:

$$SFR(\text{M}_\odot \text{yr}^{-1}) = 4.4 \times 10^{-42} L_{H\alpha} (\text{erg s}^{-1}). \quad (10.11)$$

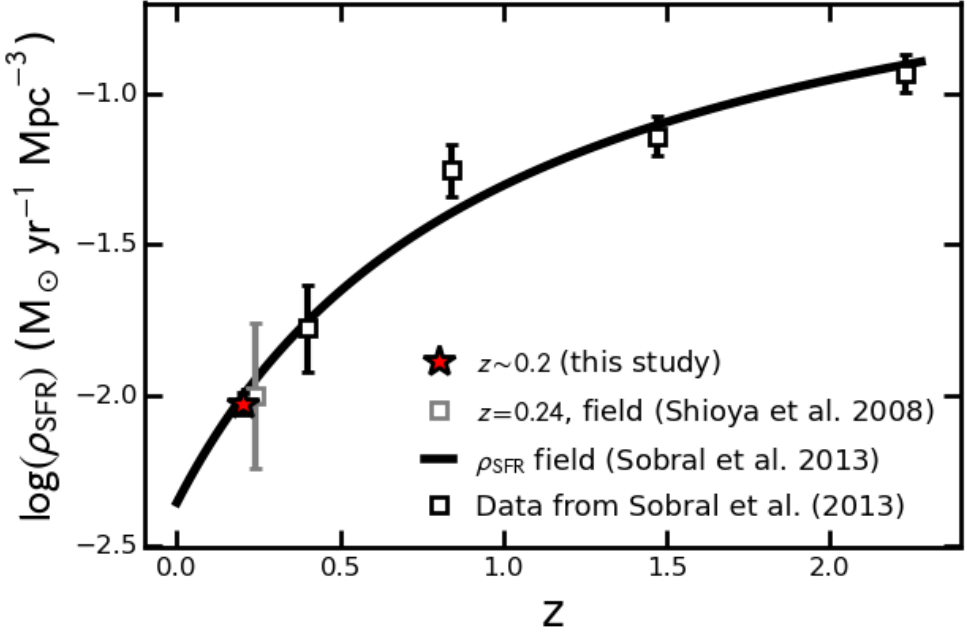


Figure 10.7: Evolution of the SFRD from $z \sim 2.23$ to $z \sim 0.2$. Our measurement at $z \sim 0.2$ confirms the previously discovered decline in SFRD, which can be simply parametrised as a function of redshift (Sobral et al. 2013).

The luminosity density is obtained by integrating the $H\alpha$ LF:

$$\rho_{L_{H\alpha}} = \int_0^{\infty} \phi(L_{H\alpha}) L_{H\alpha} dL_{H\alpha} \quad (10.12)$$

$$= \Gamma(\alpha + 2) \phi^* L_{H\alpha}^*, \quad (10.13)$$

where $\Gamma(n) = (n-1)!$ is the Gamma function. By converting from luminosity to SFR through equation 10.11, the SFRD ρ_{SFR} is:

$$\rho_{\text{SFR}} = \Gamma(\alpha + 2) \phi^* L_{H\alpha}^* 10^{0.4A_{H\alpha}} (1 - f_{\text{AGN}}) \quad (10.14)$$

where $A_{H\alpha}$ is the intrinsic $H\alpha$ dust extinction which we assume to be 1 mag and $f_{\text{AGN}} = 0.15$ is the fraction of the $H\alpha$ luminosity expected to be due to contributions from broad line and narrow line AGN emission (e.g. Garn & Best 2010; Sobral et al. 2015a).

Our measurement of the SFRD, $\rho_{\text{SFRD}} = 0.0094 \pm 0.0008 \text{ M}_{\odot} \text{yr}^{-1} \text{Mpc}^{-3}$, which matches with the value of Shioya et al. (2008) ($0.010 \pm 0.006 \text{ M}_{\odot} \text{yr}^{-1} \text{Mpc}^{-3}$). Sobral et al. (2013) derive a redshift-dependent parametrisation of the SFRD ($\rho_{\text{SFRD}} = -2.1 / (1+z) + \log 10(4.4/7.9)$), corrected for the Chabrier IMF) based on their measurements and results from Ly et al. (2007) at $z \sim 0.08$ and Shioya et al. (2008) at $z \sim 0.24$ (see Figure 10.7). Our measurement perfectly agrees with the parametrisation, which predicts a value of 0.01 at $z \sim 0.2$.

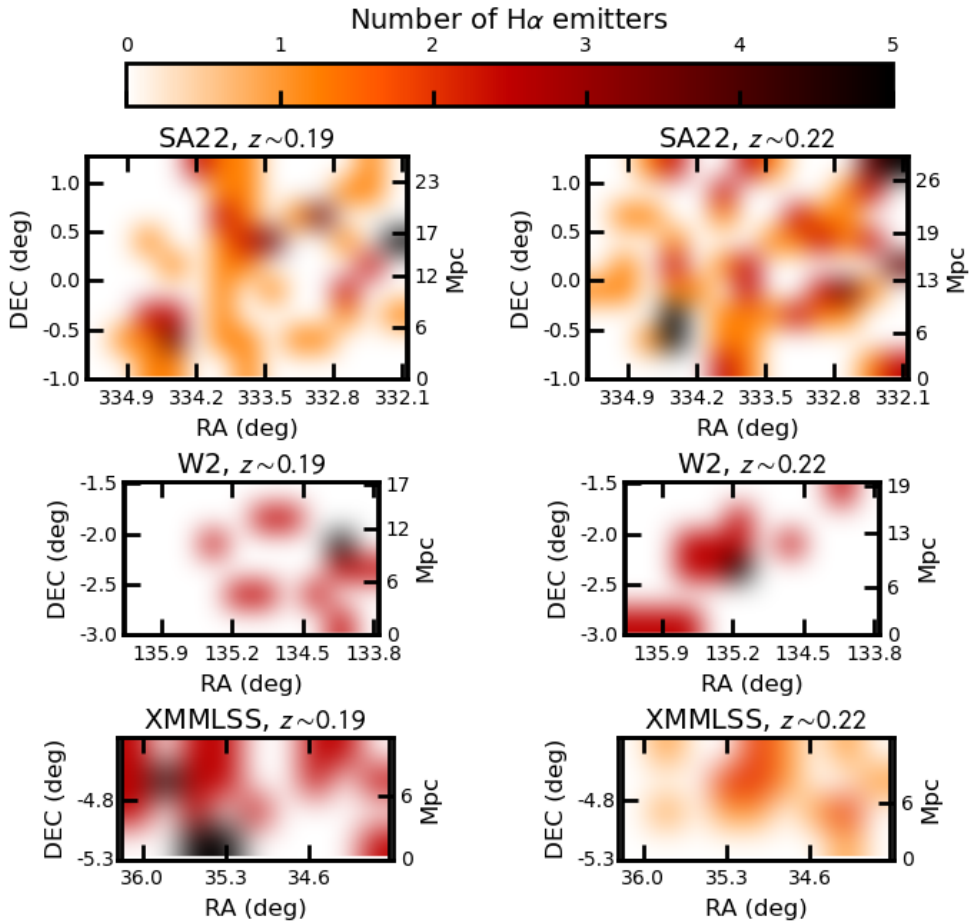


Figure 10.8: Smoothed sky distribution of the $H\alpha$ emitters. Note the amount of cosmic variance within the fields. On average 2 emitters are found per deg^2 , but the values vary between 0 and 5 sources per deg^2 .

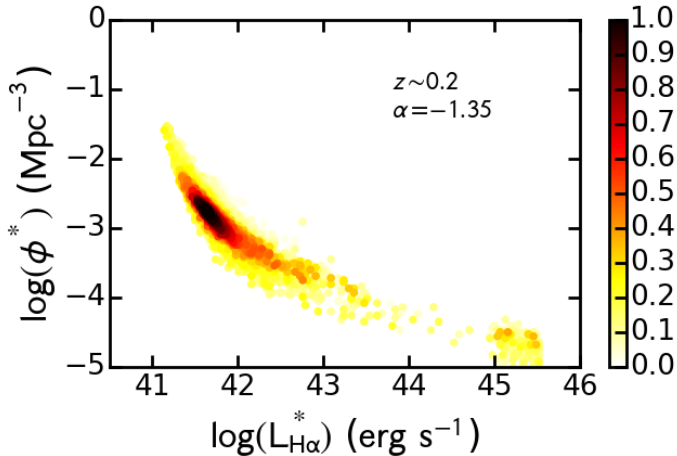


Figure 10.9: The values of LF Schechter parameters ϕ^* and $L_{H\alpha}^*$, when we fix $\alpha = -1.35$. For fitting the LF, we create 1000 random sub-samples of $H\alpha$ emitters, at a range of probed volumes. The data points are colour coded with the co-moving volume probed in units of 1000 Mpc^3 . Note how at small volumes the scatter in the value is extremely large (up to 4–5 dex), while at large volumes the values for ϕ^* and $L_{H\alpha}^*$ converge. We obtain similar results with a different value of α or when we use the data for the two filters separately (see Figure 10.16)

10.4.5 Distribution of $H\alpha$ emitters

Figure 10.8 shows the distribution of the $H\alpha$ emitters in the three fields at the two redshifts, as selected in Section 10.3.3. Note the high degree of cosmic variance within and between the field and at the adjacent redshifts.

On average, down to a limiting $H\alpha$ luminosity of $10^{41.4} \text{ erg s}^{-1}$ or $SFR \sim 1 M_{\odot} \text{ yr}^{-1}$, we find ~ 2 $H\alpha$ emitters per square degree (or ~ 3 per Mpc^3). However, there are large areas with no emitters, while parts of the W2 and XMMLSS fields have densities of up to 20 sources per square degree. The ‘Sausage’ massive, young post-merger galaxy cluster Stroe et al. (2014, 2015), where $H\alpha$ emitters were selected with the NB1 filter, was found to be extremely dense in star-forming galaxies and AGN, compared to blank fields. Down to the faintest $H\alpha$ luminosities as our current data surveys ($10^{41.1} \text{ erg s}^{-1}$), the density is ~ 140 emitters per square degree, about 70 times above the average we find over an area of 20 deg^2 . Assuming Poissonian noise, the ‘Sausage’ cluster overdensity is significant at the $> 11\sigma$ level.

The older ‘Toothbrush’ galaxy cluster merger, where the two subclusters collided about 2 Gyr ago, behaves differently. The density is about ~ 16 emitters per square degree, densities similar to the densest parts of our wide, shallow $H\alpha$ survey. Our results thus corroborate the conclusions from Stroe et al. (2014) and Stroe et al. (2015).

10.4.6 Quantifying cosmic variance

One of our goals is to understand the impact of cosmic variance and low number statistics on the determination of the LF parameters, especially motivated by the differences in LF found with the previous studies of Ly et al. (2007) and Drake et al. (2013). We generate random

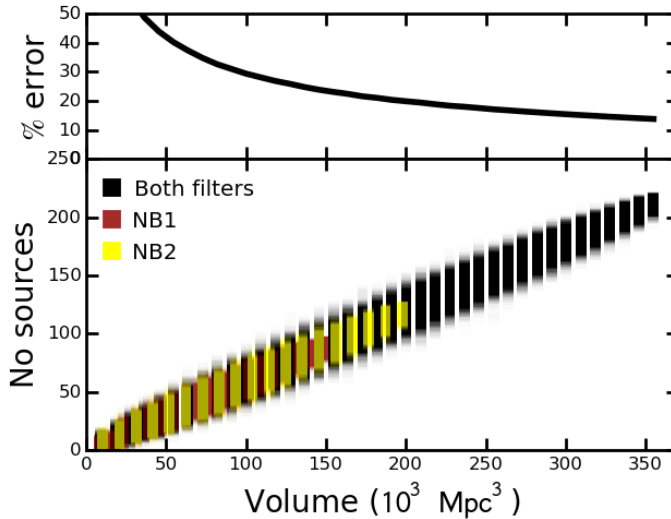


Figure 10.10: Distribution of the number of $H\alpha$ emitters randomly selected within a range of volumes. As expected the larger the volume, the larger the number of sources, with a spread at each volume size caused by cosmic variance. The Poissonian error relative to the mean number of sources does not dominate over the spread caused by cosmic variance, except where cosmic variance is minimised through the sampling of a large volumes.

subsamples of $H\alpha$ emitters, probing a range of volumes. We perform 1000 realisations starting from the smallest volumes for which we can fit a LF, up to the entire volume of our survey. We perform this experiment using $H\alpha$ emitters in each NB filter and also combine all the data together, following Sobral et al. (2015b).

The number of sources for each realisation is plotted in Figure 10.10. As expected the average number of sources increases with the volume surveyed. We calculate the standard deviation of the spread in number of sources at each volume and compare that to the Poissonian error. In the calculation of the Poissonian error we take into account the fact that the sources are divided into bins. At very low volumes, the relative Poissonian error dominates over the spread in the number of sources, which is caused by cosmic variance. Given the depth of our survey, at the very small volumes ($< 2 \times 10^4 \text{ Mpc}^3$) the Poissonian error essentially goes to infinity. Overall, the total relative error, calculated as the sum in quadrature of the Poissonian and cosmic variance error, goes down with increasing volume.

Naturally, when surveying a smaller volume, the number of $H\alpha$ sources is proportionally smaller. We therefore adapt the number of bins (N), the bin width $\Delta \log L_{H\alpha}$ and the starting bin $\log L_{H\alpha}$, depending on the volume V probed, as detailed in Table 10.5.

The results from the different realisations of the LF calculated from $H\alpha$ emitters extracted over a range of volumes can be found in Figure 10.9. At small volumes ($< 4 \times 10^4 \text{ Mpc}^3$), the random realisations of the LF give wildly different results, with values spanning 4–5 dex. This is driven by two main factors: low number statistics and cosmic variance. The low number of $H\alpha$ emitters in small volumes imposes wide and few $L_{H\alpha}$ bins to gain enough number statistics. With few bins, the LF function is barely constrained. Additionally, small volumes

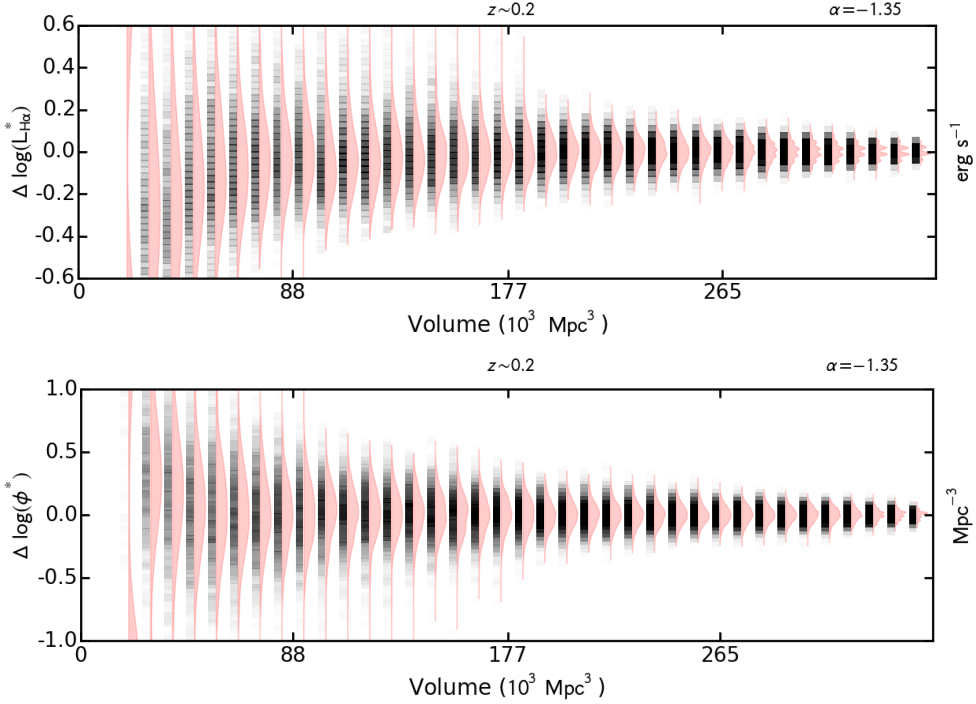


Figure 10.11: The error distribution of the characteristic $H\alpha$ luminosity $L_{H\alpha}^*$ and number density ϕ^* , as function of the volume probed. The error is calculated as fitted value minus the mean of the distribution at each volume. The results are obtained when combining data from both NB filters, with faint end slope fixed to -1.35 (see Figures 10.17, 10.18 and 10.19 for results for other α and for the two filters independently). At each volume, 1000 realisations are performed, based on random samples of sources. Each figure shows the values obtained from the LF fitting in gray-black stripe. Darker colours mean more of the realisations found that particular $L_{H\alpha}^*$ or ϕ^* value. The violin plot next to each stripe encodes the $L_{H\alpha}^*/\phi^*$ histogram. The top panel shows the standard deviation σ of the $L_{H\alpha}^*$ values at each volume size. Note that spread of values drops the larger the volume probed, indicating a convergence in the values of $L_{H\alpha}^*$ and ϕ^* .

Table 10.5: Bin width $\Delta \log L_{H\alpha}$, starting bin $\log L_{Hff,min}$ and number of bins (N) chosen for studying the luminosity function, depending on the volume V probed.

V range	$\Delta \log L_{H\alpha}$	$\log L_{Hff,min}$	N_{bins}
$< 2 \times 10^4 \text{ Mpc}^3$	0.3	41.5	4
$2 \times 10^4 - 9 \times 10^5 \text{ Mpc}^3$	0.2	41.5	4
$9 \times 10^5 - 18 \times 10^5 \text{ Mpc}^3$	0.15	41.4	5
$18 \times 10^5 - 27 \times 10^4 \text{ Mpc}^3$	0.15	41.4	6
$> 27 \times 10^5 \text{ Mpc}^3$	0.1	41.4	8

do not fully sample the LF at the brightest $L_{\text{H}\alpha}$, where H α emitters are rare. Therefore, when the volumes are small cosmic variance is significant. However, with the increase of the probed volume, we can much better constrain ϕ^* and $L_{\text{H}\alpha}^*$ parameters, by overcoming both Poissonian errors and cosmic variance. This is exemplified in Figure 10.11. The standard deviation of the $L_{\text{H}\alpha}^*$ and ϕ^* parameters at each volume size becomes smaller with increasing volume. Note however the values of $L_{\text{H}\alpha}^*$ and ϕ^* are highly correlated (Figure 10.16).

As shown in this section, cosmic variance can fully explain the differences found in the literature regarding the H α LF at $z \sim 0.2$. By accounting for cosmic variance our LF results can be reconciled with those of Drake et al. (2013) and Ly et al. (2007). Our results indicate that at $z \sim 0.2$, volumes of at least 10^5 Mpc^3 are required to overcome cosmic variance.

10.5 Clustering of H α emitters

To study the clustering of our sample of 220 bright H α emitters at $z \sim 0.2$, we start by generating a random catalogue with 1 million sources. The random catalogue sources follow the geometry of the actual observed fields and masked areas (due to saturated stars) and their number in each CCD of each pointing is normalised according to the depth attained (and hence the density of sources in that area).

We follow the method described in detail in Sobral et al. (2010), which evaluates the two-point angular correlation function minimum variance estimator proposed by Landy & Szalay (1993):

$$\omega(\theta) = 1 + \left(\frac{N_R}{N_D}\right)^2 \frac{\text{DD}(\theta)}{\text{RR}(\theta)} - 2 \frac{N_R}{N_D} \frac{\text{DR}(\theta)}{\text{RR}(\theta)}, \quad (10.15)$$

where θ is the angle on the sky and N_R and N_D are the number of sources in the random and real catalogue of H α sources. $\text{DD}(\theta)$, $\text{RR}(\theta)$ and $\text{DR}(\theta)$ are the number pairs of sources located at distances between θ and $\theta + \delta\theta$ in the real data, random data and between real and random data, respectively.

Errors on $\omega(\theta)$ are then (Landy & Szalay 1993):

$$\Delta\omega(\theta) = \frac{1 + \omega(\theta)}{\sqrt{\text{DD}(\theta)}}. \quad (10.16)$$

We determine $\omega(\theta)$ using 1000 different randomly selected sub-samples of sources selected from the randomly generated catalogue. We perform our analysis separately on emitters selected in each filter, but combine the data for the SA22, W2 and XMMLSS fields. We use the full luminosity range ($L_{\text{H}\alpha} = 10^{41.0-42.4} \text{ erg s}^{-1}$) of the H α emitters, as well as split the sample in two roughly equal halves: a faint sample with luminosities in the range $10^{41.0-41.55} \text{ erg s}^{-1}$ and a bright one with luminosities $10^{41.55-42.40} \text{ erg s}^{-1}$. We bin the data using a range of angular scale bins (with different starting bin θ_{min} , bin width $\delta\theta$ and maximum bin θ_{max}).

The results are presented in Figure 10.12 and Table 10.6. The two-point correlation function for the samples is well described by a single power law. The results for the two filters are considered separately and when combined give fully consistent results within the error bars.

Note we studied only the range $0.02 \text{ deg} < \theta < 3.0 \text{ deg}$, where there was enough signal. At scales smaller than $< 0.02 \text{ deg}$, a flattening of $\omega(\theta)$ occurs, maybe caused by bright H α emitters not being able to reside in a single halo. Additionally, since our survey is not very

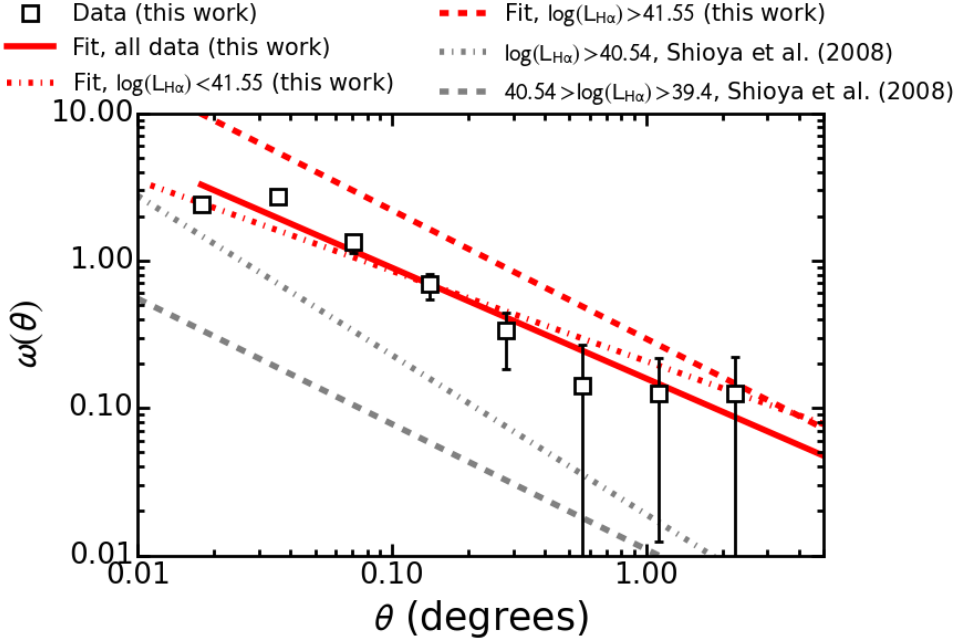


Figure 10.12: Angular two-point correlation function for bright $H\alpha$ emitters ($L_{H\alpha} \gtrsim 10^{41.0}$ erg s^{-1}) at $z \sim 0.2$. The best fit power law relation is: $\omega(\theta) = (0.109 \pm 0.005)\theta^{(-0.79 \pm 0.04)}$. For comparison, we plot the results for fainter emitters ($L_{H\alpha} \lesssim 10^{41.5}$ erg s^{-1}) from Shioya et al. (2008). We find that more luminous $H\alpha$ emitters are more clustered.

Table 10.6: Two-point correlation function for $H\alpha$ emitters at $z \sim 0.2$. Best fit as a single power law of the form $\omega(\theta) = A\theta^\beta$. Note that the filters and redshift distribution is different for Shioya et al. (2008) than for our study, so the amplitudes cannot be directly compared.

Source	$\log(L_{H\alpha})$ (erg s^{-1})	A	β
This study	41.00 – 42.40	0.159 ± 0.012	-0.75 ± 0.05
Faint	41.00 – 41.55	0.208 ± 0.035	-0.61 ± 0.07
Bright	41.55 – 42.40	0.295 ± 0.026	-0.87 ± 0.06
Shioya et al. (2008)	40.54 – 41.50	0.019 ± 0.004	-1.08 ± 0.05
Shioya et al. (2008)	39.40 – 40.54	0.011 ± 0.002	-0.85 ± 0.05

deep, we do not probe the regime where satellites are expected. Therefore, we cannot evaluate the departure of the two-point correlation function from a single power, which is caused by the transition from the large scale (two galaxies residing in separate dark matter halo) to the small scale clustering regime (galaxies sharing a single halo, e.g. Ouchi et al. 2005).

Previous research indicates that bright $H\alpha$ galaxies as well as Lyman break galaxies are more clustered than the faint ones. Shioya et al. (2008) found that the two-point correlation function for faint $H\alpha$ emitters ($L_{H\alpha} < 10^{40.54}$ erg s $^{-1}$) at $z \sim 0.24$ follows the relationship: $\omega(\theta) = (0.011 \pm 0.002)\theta^{(-0.84 \pm 0.05)}$, while brighter emitters with $10^{40.54} < L_{H\alpha} \lesssim 10^{41.5}$ erg s $^{-1}$ follow the relationship: $\omega(\theta) = (0.019 \pm 0.004)\theta^{(-1.08 \pm 0.05)}$. The amplitude of the two-point correlation function for our faint sample is 0.208 ± 0.035 , while for the bright sample it is slightly larger: 0.295 ± 0.026 . The relation is also steeper for the bright sample than for the faint sample. Our results therefore support and extend the claim that brighter (and hence more star-forming galaxies) are more clustered than faint ones to very high luminosities beyond $10^{41.0}$ erg s $^{-1}$ up to $10^{42.4}$ erg s $^{-1}$ ($L/L_{H\alpha}^* \sim 5.0$).

We use the inverse Limber transformation and the redshift distribution of the NB filters to translate the two-point correlation function into a 3D spatial correlation (Peebles 1980), assuming the latter is well described by $\epsilon = (r/r_0)^\gamma$, where r_0 is the real-space correlation length of the $H\alpha$ emitters. Following the method of Sobral et al. (2010), we assume that the two filters have a perfect top-hat shape. We compute r_0 for each realisation of $\omega(\theta)$ in each filter, by fixing $\beta = -0.8$. We finally combine the data for the two filters. The dependence of r_0 on redshift is shown in Figure 10.13.

For the full sample, we obtain a correlation length $r_0 = 3.3$ Mpc/h with a standard deviation 0.8 Mpc/h. We obtain $r_0 = 3.5 \pm 1.1$ Mpc/h for our fainter $H\alpha$ sample and 5.0 ± 1.5 Mpc/h for the brighter one. Our measurements are larger than those of Sobral et al. (2010) at $z \sim 0.24$ (based on the sample from Shioya et al. (2008)), which find a value of 1.8 ± 0.2 Mpc/h for their sample with $10^{39.4} < L_{H\alpha} < 10^{41.5}$ erg s $^{-1}$. As expected, fainter $H\alpha$ galaxies have smaller correlation lengths than brighter ones (Norberg et al. 2001; Shioya et al. 2008; Sobral et al. 2010). The correlation length also depends on redshift, but the evolution is driven by the typical luminosity: at high redshift, $H\alpha$ emitters are on average brighter and have larger r_0 than lower redshift sources.

Similar results are found by Hartley et al. (2010), who select galaxies using K band luminosity as proxy for stellar mass. The authors find that red galaxies, likely mostly ellipticals, are more clustered than the blue galaxies. Selecting star-forming galaxies based on colours, they find that r_0 drops with redshift. However, no dependence of r_0 on broad band luminosity was found. By contrast, Bielby et al. (2014) use a mass selected sample and find that higher mass galaxies tend to have larger clustering lengths. Additionally, they find that the clustering strength increases with stellar mass. Stellar mass correlates well with SFR (e.g. at $z \sim 0.2$ Stroe et al. 2015), which can then be translated to an equivalent $H\alpha$ luminosity through equation 10.11. The results from Bielby et al. (2014) may indicate that more star forming, more luminous galaxies have larger r_0 which is consistent with our findings. Note however that Sobral et al. (2010) controlled for both $H\alpha$ luminosity and mass (K band luminosity) and found both are important for the evolution of r_0 : r_0 increases with both higher $L_{H\alpha}$ and K band luminosity.

The clustering of the $H\alpha$ emitters depends on the clustering of their host dark matter (DM) haloes. The bias parameter $b(z)$ describes how the matter distribution traces the DM

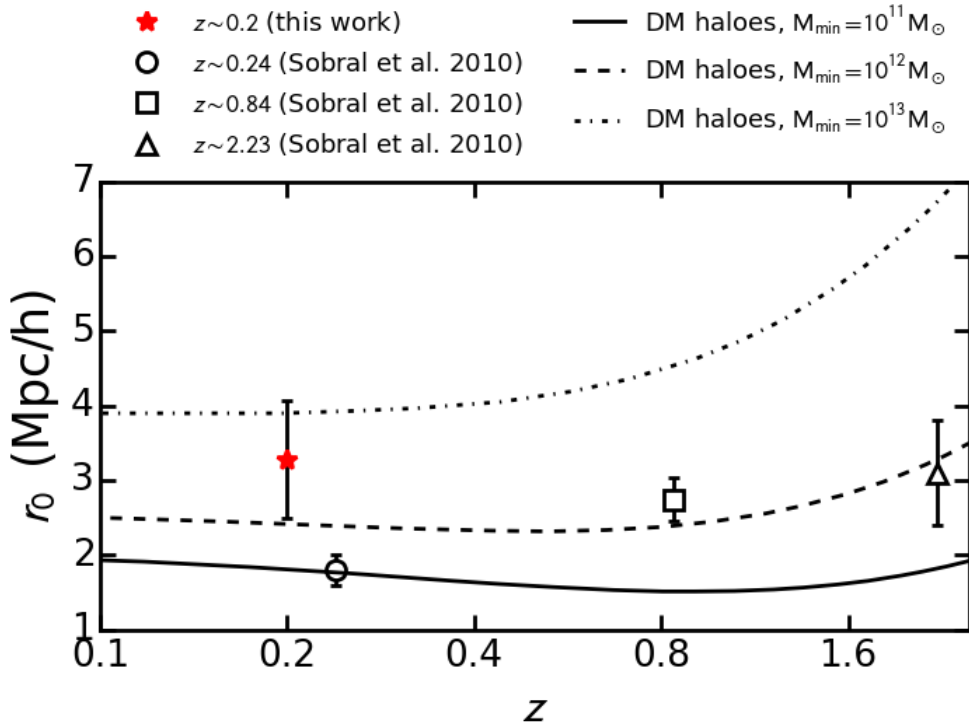


Figure 10.13: The dependence of the clustering length r_0 on redshift, using a consistent set of $H\alpha$ emitters selected through NB surveys. For comparison, we are also showing data from Sobral et al. (2010). The plot suggests that typical ($L_{H\alpha}^*$) emitters have very similar r_0 across cosmic time. At $z \sim 0.2$, there is a sharp increase in the typical DM halo mass with luminosity of the $H\alpha$ sample. Note however, as shown in Figure 10.14, that once corrected for the redshift evolution of the characteristic luminosity, $L_{H\alpha}$ sets the position of galaxies in relation to DM halo host.

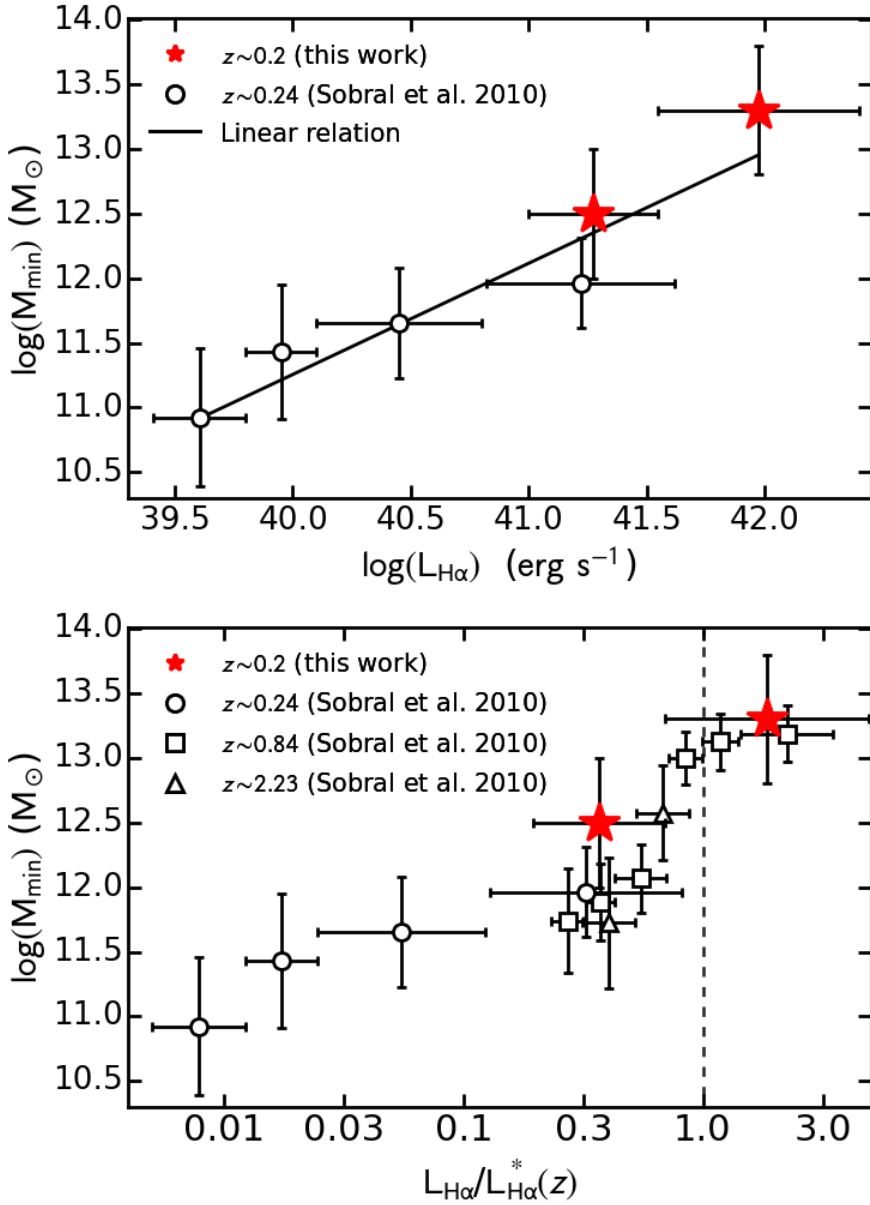


Figure 10.14: The minimum DM halo mass (M_{DM}) as function of luminosity ($L_{H\alpha}$, left) and luminosity scaled by the characteristic luminosity at the respective redshift ($L_{H\alpha}/L_{H\alpha}^*(z)$, right). The data from Sobral et al. (2010), split per luminosity bin, are shown for comparison. The ~ 0.2 points are renormalised using the $L_{H\alpha}^*$ derived in this paper. All luminosities are not corrected for intrinsic dust extinction. Note the relation between the $H\alpha$ luminosity and host mass. When scaled for the typical luminosity, a clear relation between DM halo mass and luminosity is observed from $z \sim 2.23$ to $z \sim 0.2$.

distribution, as function of redshift. In the bias model of Matarrese et al. (1997), the physical parameters of galaxies are determined by their host dark matter halo mass. In such a model, $b(z)$ depends on the minimum mass of the DM halo. Figure 10.13 also contain r_0 predictions for dark matter (DM) haloes with fixed minimum mass of $M_{\min} = 10^{11-13} M_{\odot}$, as calculated by Geach et al. (2008) assuming a Λ CDM cosmology and an evolving bias model from Matarrese et al. (1997) and Moscardini et al. (1998). Note however, the r_0 prediction is highly dependent on the model, see for example Hartley et al. (2010). We thus note that while the trends are valid, the normalisation of the M_{\min} could be higher than that used here, leading to lower masses than derived here.

The emitters from Shioya et al. (2008), probing fainter H α regimes with $L_{\text{H}\alpha} < 10^{41.5}$ erg s $^{-1}$, reside in DM haloes of $10^{11} M_{\odot}$ mass. These are most likely dwarf galaxies. By contrast, our faint sample is hosted by DM haloes of about $10^{12.5} M_{\odot}$ mass, about the mass of the Milky Way. The bright H α emitters are hosted by $\sim 10^{13-13.5} M_{\odot}$ DM haloes, which are most probably already galaxy groups.

Figure 10.14 shows how the DM halo minimum mass varies as function of H α luminosity and the luminosity scaled by the characteristic luminosity at that redshift ($L_{\text{H}\alpha}/L_{\text{H}\alpha}^*(z)$). By comparing our results, with the results from Sobral et al. (2010) (based on data from Shioya et al. (2008)), we find a linear correlation between the host minimum DM halo mass and luminosity (in log-log space, see Figure 10.14). This indicates that more luminous, more star-forming galaxies reside in more massive dark matter haloes.

Accounting for the evolution of the characteristic luminosity with redshift, we find that more luminous emitters reside in more massive DM haloes, irrespective of redshift. Such a comparison between $z < 0.4$ and $z > 4$ samples has been previously difficult because of the different $L_{\text{H}\alpha}/L_{\text{H}\alpha}^*(z)$ ranges probed in the different redshift ranges. With our measurements, we probe beyond $L_{\text{H}\alpha}^*$ at $z \sim 0.2$ for the first time to be fully comparable with samples up to $z \sim 2.23$. Our measurements therefore confirm the results from Sobral et al. (2010) and Geach et al. (2012), who find that $L_{\text{H}\alpha}^*$ galaxies reside in $\sim 10^{13} M_{\odot}$, Milky Way size DM haloes, at all redshifts. The results indicate the the position of a star forming galaxies within the H α luminosity function is dictated by the host DM halo mass, at all cosmic times since ~ 2.3 .

10.6 Conclusions

In order to constrain the evolution of the star-forming galaxies across cosmic time, large samples of sources are necessary. Such samples are available at high redshifts ($z > 0.8$) through NB selected H α emitter samples which probe large volumes ($> 10^5 \text{ Mpc}^3$) and overcome cosmic variance. However, at low redshifts ($z < 0.8$), large areas ($> 15 \text{ deg}^2$) need to be surveyed in order to match the volumes at high redshift. By carrying out the largest survey of H α emitters at $z \sim 0.2$, we produce a luminosity function describing typical galaxies within representative volumes of the Universe. With our large sample of bright emitters we study their distribution and clustering and place it in the context of the evolution of the SFRD throughout cosmic history. Our main results are:

- The H α luminosity function at $z \sim 0.2$ is well described by a Schechter function with $\log(\phi^*) = -2.85 \pm 0.03 \text{ (Mpc}^{-3}\text{)}$ and $\log(L_{\text{H}\alpha}^*) = 41.71 \pm 0.02 \text{ (erg s}^{-1}\text{)}$. We find that previous studies, probing far smaller volumes, underestimate the characteristic luminos-

ity $L_{H\alpha}^*$, but are reconciled with our results if cosmic variance uncertainties are taken into account. For volumes typically probed in previous $H\alpha$ works at $z \sim 0.2$ of $< 5 \times 10^4 \text{ Mpc}^3$, cosmic variance can account to more than 50 per cent variance in the LF parameters.

- By assuming a 15 per cent AGN fraction, we derive a star formation rate density of $\rho_{\text{SFRD}} = 0.0094 \pm 0.0008 \text{ M}_{\odot} \text{ yr}^{-1} \text{ Mpc}^{-1}$.
- We find significant cosmic variance in the distribution of the $H\alpha$ emitters, but on average 1–4 bright ($L_{H\alpha} > 10^{41.1} \text{ erg s}^{-1}$) $H\alpha$ emitters are found per square degree.
- We study the clustering of the $H\alpha$ emitters. The two-point correlation function is well fit by a single power law $\omega(\theta) = (0.159 \pm 0.012)\theta^{(-0.75 \pm 0.05)}$, with a spatial clustering length $r_0 = 5.0 \pm 1.1 \text{ Mpc/h}$ for the bright sample ($10^{41.0-41.55} \text{ erg s}^{-1}$) and $r_0 = 3.5 \pm 1.1 \text{ Mpc/h}$ for the faint sample ($10^{41.55-42.40} \text{ erg s}^{-1}$). Our results confirm that luminous, strongly star-forming galaxies are more clustered than those weakly star-forming.
- We find that, at $z \sim 0.2$, the higher the SFR, the more massive the DM halo host is. When accounting for the redshift dependence of the characteristic $H\alpha$ luminosity, there is no redshift dependence of the host mass, but a strong dependence on $L_{H\alpha}/L_{H\alpha}^*(z)$.

Acknowledgements

We thank the referee for comments which improved the clarity and interpretation of our results. Based on observations made with the Isaac Newton Telescope (proposal I13BN008) operated on the island of La Palma by the Isaac Newton Group in the Spanish Observatorio del Roque de los Muchachos of the Instituto de Astrofísica de Canarias. Based on observations obtained with MegaPrime/MegaCam, a joint project of CFHT and CEA/IRFU, at the Canada-France-Hawaii Telescope (CFHT) which is operated by the National Research Council (NRC) of Canada, the Institut National des Science de l'Univers of the Centre National de la Recherche Scientifique (CNRS) of France, and the University of Hawaii. This work is based in part on data products produced at Terapix available at the Canadian Astronomy Data Centre as part of the Canada-France-Hawaii Telescope Legacy Survey, a collaborative project of NRC and CNRS. Based on observations obtained as part of the VISTA Hemisphere Survey, ESO Program, 179.A-2010 (PI: McMahon). Based on data products from observations made with ESO Telescopes at the La Silla or Paranal Observatories under ESO programme ID 179.A-2006. The UKIDSS project is defined in Lawrence et al. (2007). UKIDSS uses the UKIRT Wide Field Camera (WFCAM; Casali et al. 2007). The photometric system is described in Hewett et al. (2006), and the calibration is described in Hodgkin et al. (2009). The pipeline processing and science archive are described in Irwin et al (2009, in prep) and Hambly et al (2008). This research has made use of the NASA/IPAC Extragalactic Database (NED) which is operated by the Jet Propulsion Laboratory, California Institute of Technology, under contract with the National Aeronautics and Space Administration. This research has made use of NASA's Astrophysics Data System. AS acknowledges financial support from an NWO top subsidy (614.001.006). DS acknowledges financial support from the Netherlands Organisation for Scientific research (NWO) through a Veni fellowship, from FCT through

a FCT Investigator Starting Grant and Start-up Grant (IF/01154/2012/CP0189/CT0010) and from FCT grant PEst-OE/FIS/UI2751/2014.

Bibliography

- Ahn, C. P., Alexandroff, R., Allende Prieto, C., et al. 2012, *ApJS*, 203, 21
- Bertin, E., & Arnouts, S. 1996, *A&AS*, 117, 393
- Bertin, E., Mellier, Y., Radovich, M., et al. 2002, *Astronomical Data Analysis Software and Systems XI*, 281, 228
- Bertin, E. 2006, *Astronomical Data Analysis Software and Systems XV*, 351, 112
- Best, P., Smail, I., Sobral, D., et al. 2010, arXiv:1003.5183
- Bielby, R. M., Gonzalez-Perez, V., McCracken, H. J., et al. 2014, *A&A*, 568, A24
- Bland-Hawthorn, J., van Breugel, W., Gillingham, P. R., Baldry, I. K., & Jones, D. H. 2001, *ApJ*, 563, 611
- Bouwens, R. J., Illingworth, G. D., Oesch, P. A., et al. 2011, *ApJ*, 737, 90
- Bouwens, R. J., Illingworth, G. D., Oesch, P. A., et al. 2015, *ApJ*, 803, 34
- Bunker, A. J., Warren, S. J., Hewett, P. C., & Clements, D. L. 1995, *MNRAS*, 273, 513
- Casali, M., Adamson, A., Alves de Oliveira, C., et al. 2007, *A&A*, 467, 777
- Chabrier, G. 2003, *PASP*, 115, 763
- Dale, D. A., Barlow, R. J., Cohen, S. A., et al. 2010, *ApJL*, 712, L189
- Drake, A. B., Simpson, C., Collins, C. A., et al. 2013, *MNRAS*, 433, 796
- Dressler, A. 1980, *ApJ*, 236, 351
- Drury, L. O. 1983, *Reports on Progress in Physics*, 46, 973
- Erben, T., Hildebrandt, H., Miller, L., et al. 2013, *MNRAS*, 433, 2545
- Garcet, O., Gandhi, P., Gosset, E., et al. 2007, *A&A*, 474, 473
- Garn, T., & Best, P. N. 2010, *MNRAS*, 409, 421
- Geach, J. E., Smail, I., Best, P. N., et al. 2008, *MNRAS*, 388, 1473
- Geach, J. E., Sobral, D., Hickox, R. C., et al. 2012, *MNRAS*, 426, 679
- Gunawardhana, M. L. P., Hopkins, A. M., Bland-Hawthorn, J., et al. 2013, *MNRAS*, 433, 2764
- Gwyn, S. D. J. 2012, *AJ*, 143, 38

- Hartley, W. G., Almaini, O., Cirasuolo, M., et al. 2010, MNRAS, 407, 1212
- Hewett, P. C., Warren, S. J., Leggett, S. K., & Hodgkin, S. T. 2006, MNRAS, 367, 454
- Hodgkin, S. T., Irwin, M. J., Hewett, P. C., & Warren, S. J. 2009, MNRAS, 394, 675
- Ilbert, O., Arnouts, S., McCracken, H. J., et al. 2006, A&A, 457, 841
- Jarvis, M. J., Bonfield, D. G., Bruce, V. A., et al. 2013, MNRAS, 428, 1281
- Karim, A., Schinnerer, E., Martínez-Sansigre, A., et al. 2011, ApJ, 730, 61
- Kennicutt, R. C., Jr. 1998, ARA&A, 36, 189
- Kirkpatrick, J. D., Henry, T. J., & McCarthy, D. W., Jr. 1991, ApJS, 77, 417
- Kirkpatrick, J. D., Reid, I. N., Liebert, J., et al. 1999, ApJ, 519, 802
- Kurk, J. D., Pentericci, L., Röttgering, H. J. A., & Miley, G. K. 2004, A&A, 428, 793
- Landy, S. D., & Szalay, A. S. 1993, ApJ, 412, 64
- Lawrence, A., Warren, S. J., Almaini, O., et al. 2007, MNRAS, 379, 1599
- Lilly, S. J., Le Fevre, O., Hammer, F., & Crampton, D. 1996, ApJL, 460, L1
- Ly, C., Malkan, M. A., Kashikawa, N., et al. 2007, ApJ, 657, 738
- Matarrese, S., Coles, P., Lucchin, F., & Moscardini, L. 1997, MNRAS, 286, 115
- Matthee, J. J. A., Sobral, D., Swinbank, A. M., et al. 2014, MNRAS, 440, 2375
- Melnyk, O., Plionis, M., Elyiv, A., et al. 2013, A&A, 557, AA81
- Moorwood, A. F. M., van der Werf, P. P., Cuby, J. G., & Oliva, E. 2000, A&A, 362, 9
- Moscardini, L., Coles, P., Lucchin, F., & Matarrese, S. 1998, MNRAS, 299, 95
- Naylor, T. 1998, MNRAS, 296, 339
- Norberg, P., Baugh, C. M., Hawkins, E., et al. 2001, MNRAS, 328, 64
- Ouchi, M., Shimasaku, K., Akiyama, M., et al. 2005, ApJL, 620, L1
- Peebles, P. J. E. 1980, Research supported by the National Science Foundation. Princeton, N.J., Princeton University Press, 1980. 435 p.
- Pierre, M., Valtchanov, I., Altieri, B., et al. 2004, JCAP, 9, 011
- Polletta, M., Tajer, M., Maraschi, L., et al. 2007, ApJ, 663, 81
- Roberts, M. S. 1962, AJ, 67, 437
- Schechter, P. 1976, ApJ, 203, 297
- Shioya, Y., Taniguchi, Y., Sasaki, S. S., et al. 2008, ApJS, 175, 128

- Sobral, D., Best, P. N., Geach, J. E., et al. 2009, MNRAS, 398, 75
- Sobral, D., Best, P. N., Geach, J. E., et al. 2010, MNRAS, 404, 1551
- Sobral, D., Best, P. N., Matsuda, Y., et al. 2012, MNRAS, 420, 1926
- Sobral, D., Smail, I., Best, P. N., et al. 2013, MNRAS, 428, 1128
- Sobral, D., Best, P. N., Smail, I., et al. 2014, MNRAS, 437, 3516
- Sobral, D., Stroe, A., Dawson, W. A., et al. 2015a, MNRAS, 450, 630
- Sobral, D., Matthee, J., Best, P. N., et al. 2015b, arXiv:1502.06602
- Stott, J. P., Sobral, D., Smail, I., et al. 2013, MNRAS, 430, 1158
- Stroe, A., Sobral, D., Röttgering, H. J. A., & van Weeren, R. J. 2014, MNRAS, 438, 1377
- Stroe, A., Sobral, D., Dawson, W., et al. 2015, MNRAS, 450, 646
- Tajer, M., Polletta, M., Chiappetti, L., et al. 2007, A&A, 467, 73
- Warren, S. J., Cross, N. J. G., Dye, S., et al. 2007, arXiv:astro-ph/0703037
- Zacharias, N., Finch, C. T., Girard, T. M., et al. 2013, AJ, 145, 44

10.7 Appendix

10.7.1 Survey completeness

The method for studying the completeness is detailed in Section 10.4.1. The dependence of the completeness on line flux is shown in Figure 10.15.

10.7.2 Survey completeness

The results of the resampling of the LF at $z \sim 0.2$ with different binnings is presented for a range of data selections. The faint end slope is fixed at -1.35 and -1.7 and ϕ and L are fit using data selected from the two NB filters independently and combined. The results are shown in Figures 10.16, 10.17, 10.18 and 10.19.

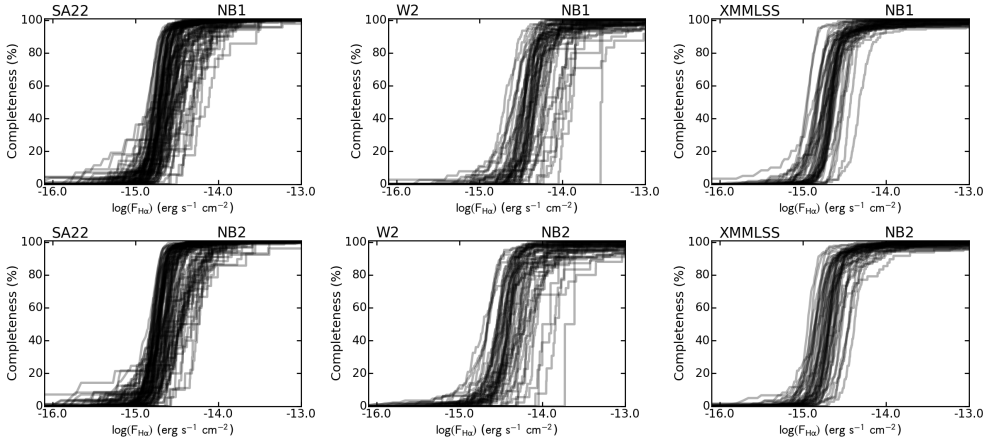


Figure 10.15: Survey completeness as a function of $H\alpha$ flux, plotted separately for each field and NB filter used to select $H\alpha$ candidates. Each curve is associated with the the completeness study for a different CCD chip within each pointing. The darker the colour the more completeness curves fall within that region. Note the XMMLSS field is significantly more complete than the W2 field.

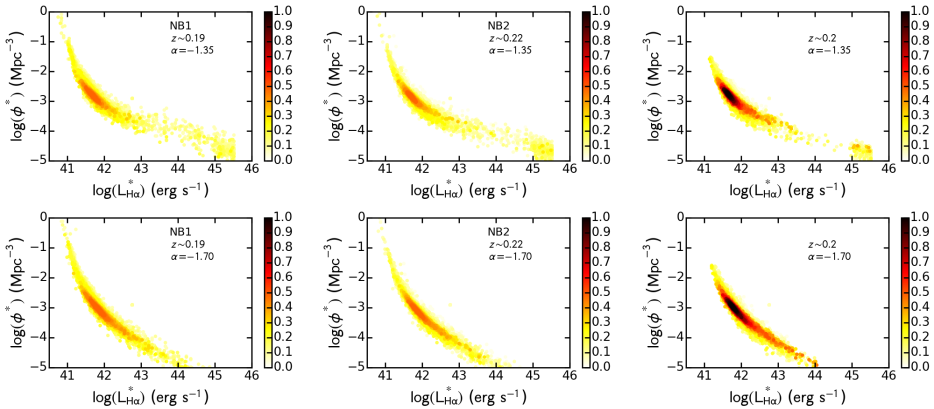


Figure 10.16: As for Figure 10.9, but with different values of α and when using the data for the two filters separately or together.

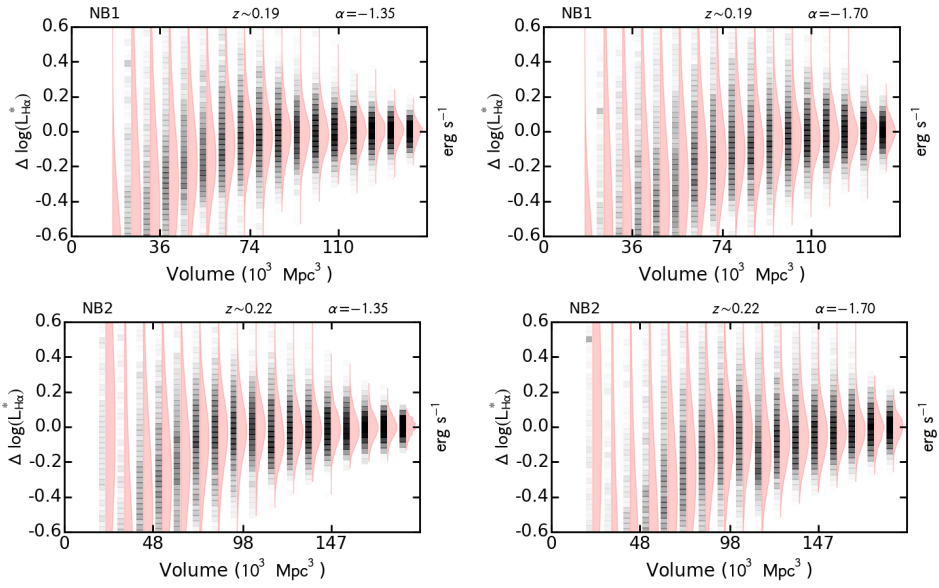


Figure 10.17: As Figure 10.11, but for data samples from the two NB filters independently. Note that similar results are found for the two filters, even when considered separately.

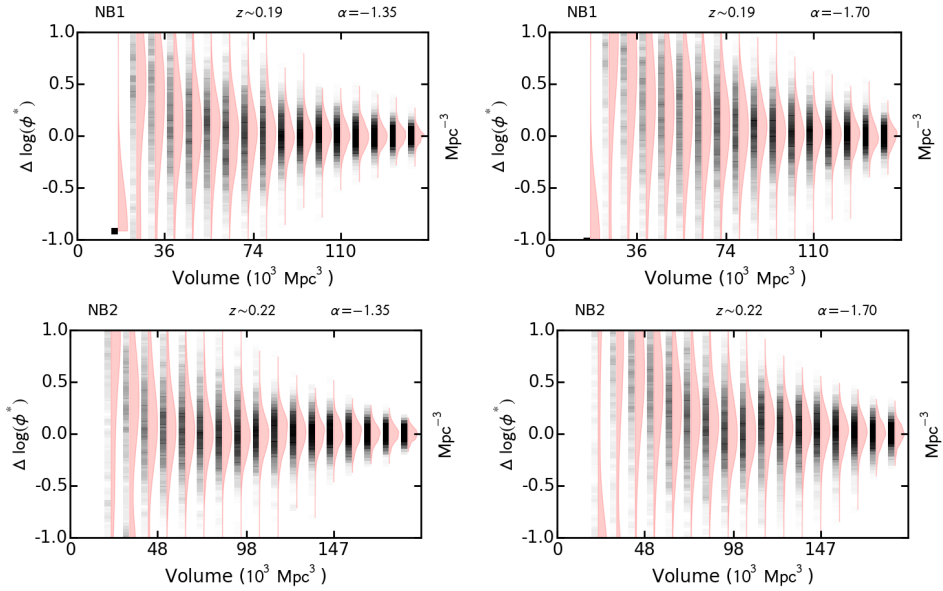


Figure 10.18: As Figure 10.11, but for data samples from the two NB filters independently. Note that similar results are found for the two filters, even when considered separately.

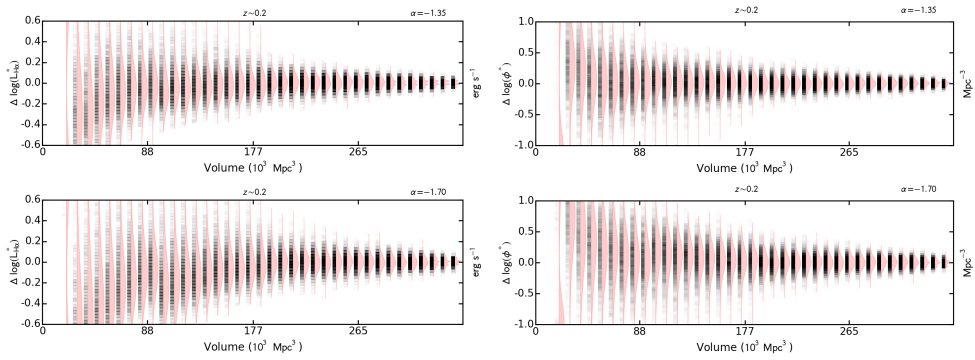


Figure 10.19: As Figure 10.11, but for different α values.